

1      **A novel formation mechanism of sulfamic acid and its enhancing**  
2      **effect on methanesulfonic acid-methylamine aerosol particle**  
3      **formation in agriculture-developed and coastal industrial areas**

4      **Hui Wang<sup>a,‡</sup>, Shuqin Wei<sup>a,‡</sup>, Jihuan Yang<sup>a</sup>, Yanlong Yang<sup>a</sup>, Rongrong Li<sup>a</sup>, Rui Wang<sup>a</sup>,**  
5      **Chongqin Zhu<sup>b,\*</sup>, Tianlei Zhang<sup>a,\*</sup>, Changming Zhang<sup>c</sup>**

6      *<sup>a</sup> Shaanxi Key Laboratory of Catalysis, School of Chemical & Environment Science, Shaanxi  
7      University of Technology, Hanzhong, Shaanxi 723001, P. R. China*

8      *<sup>b</sup> College of Chemistry, Key Laboratory of Theoretical & Computational Photochemistry of  
9      Ministry of Education, Beijing Normal University, Beijing 100190, China.*

10     *<sup>c</sup> School of Mechanical Engineering, Shaanxi University of Technology, Hanzhong, Shaanxi 723001,  
11     P. R. China*

12     **Abstract**

13     Sulfamic acid (SFA) significantly impacts atmospheric pollution and poses potential risks to human  
14     health. Although traditional source of SFA and its role on sulfuric acid-dimethylamine new particle  
15     formation (NPF) has received increasing attention, the formation mechanism of SFA from  $\text{HNSO}_2$   
16     hydrolysis with methanesulfonic acid (MSA) and its enhancing effect on MSA-methylamine (MA)  
17     NPF has not been studied, which will limit the understanding for the source and loss of SFA in  
18     agriculture-developed and coastal industrial areas. Here, the gaseous and interfacial formation of  
19     SFA from  $\text{HNSO}_2$  hydrolysis with MSA was investigated using quantum chemical calculations and  
20     BOMD simulations. Furthermore, the role of SFA in MSA-MA system was assessed using the  
21     ACDC kinetic model. Our simulation results indicate that the gaseous SFA formation from the  
22     hydrolysis of  $\text{HNSO}_2$  with MSA can be competitive with that catalyzed by  $\text{H}_2\text{O}$  within an altitude  
23     of 5-15 km. At the air-water interface, two types of reactions, the ions forming mechanism and the  
24     proton exchange mechanism to form  $\text{SFA}^{\cdot-}\cdots\text{H}_3\text{O}^+$  ion pair were observed on the timescale of  
25     picosecond. Considering the overall environment of sulfuric acid emission reduction, the present  
26     findings suggest that SFA may play a significant role in NPF and the growth of aerosol particle as  
27     *i*) SFA can directly participate in the formation of MSA-MA-based cluster and enhance the rate of  
28     NPF from these clusters by approximately  $10^3$  times at 278.15 K; and *ii*) the  $\text{SFA}^{\cdot-}$  species at the air-  
29     water interface can attract gaseous molecules to the aqueous surface, and thus promote particle  
30     growth.

---

\* Corresponding authors, Tel: +86-0916-2641083, Fax: +86-0916-2641083.

E-mail: [cqzhu@bnu.edu.cn](mailto:cqzhu@bnu.edu.cn) (C. Q. Zhu), [ztianlei88@163.com](mailto:ztianlei88@163.com) (T. L. Zhang).

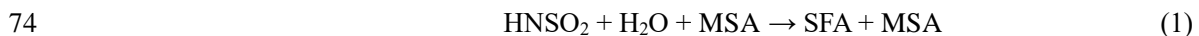
‡ These authors contributed equally to this work.

31     **1 Introduction**

32     As a well-studied nitrogen derivative of sulfuric acid (Rennebaum et al., 2024), sulfamic acid  
33 (SFA) was not only recognized as a potent aerosol and cloud nucleating agent (Xue et al., 2024;  
34 Zhang et al., 2023; Pszona et al., 2015; Li et al., 2018), but also can harm human health through  
35 atmospheric deposition into water bodies (Van Stempvoort et al., 2019). In agriculture-developed  
36 and industrial areas with high ammonia ( $\text{NH}_3$ ) concentrations, such as the Yangtze River Delta in  
37 China (Yu et al., 2020), Indo-Gangetic Plains (Kuttipurath et al., 2020), Pakistan, Bangladesh  
38 (Warner et al., 2016), and the southern Italy (Tang et al., 2021), the atmospheric concentration of  
39 SFA estimated by theoretical method of CCSD(T)-F12/cc-pVDZ-F12//M06-2X/6-311++G(3df,3pd)  
40 (Li et al., 2018) was expected to reach up to  $10^8$  molecules· $\text{cm}^{-3}$ , and thus lead to it becoming a  
41 significant air pollutant. So, the sources of SFA in the atmosphere has been focused by several  
42 groups (Lovejoy and Hanson, 1996; Pszona et al., 2015; Li et al., 2018; Larson and Tao, 2001;  
43 Manonmani et al., 2020; Zhang et al., 2022). The traditional source of SFA was mainly taken from  
44 the ammonolysis of  $\text{SO}_3$  (Lovejoy and Hanson, 1996; Larson and Tao, 2001; Li et al., 2018).  
45 Experimentally, the rate coefficient for the ammonolysis of  $\text{SO}_3$  was detected to be  $2.0 \times 10^{-11}$   
46  $\text{cm}^3 \cdot \text{molecules}^{-1} \cdot \text{s}^{-1}$  at 295 K (Lovejoy and Hanson, 1996), which was close to the value for the  
47 hydrolysis of  $\text{SO}_3$  assisted by water molecule ( $10^{-11}\text{--}10^{-10} \text{ cm}^3 \text{ molecule}^{-1} \text{ s}^{-1}$ ) (Kim et al., 1998;  
48 Hirota et al., 1996; Shi et al., 1994; Kolb et al., 1994; Long et al., 2013; Long et al., 2023; Ding et  
49 al., 2023; Cheng et al., 2023; Wang et al., 2024). Theoretically, the ammonolysis of  $\text{SO}_3$  to produce  
50 SFA can be catalyzed by  $\text{NH}_3$ . In arid and heavily polluted regions with high  $\text{NH}_3$  concentrations,  
51 the effective rate coefficient for the ammonolysis of  $\text{SO}_3$  can be sufficiently rapid, making it  
52 competitive with the conventional loss pathway of  $\text{SO}_3$  with water (Li et al., 2018).

53     In addition to the ammonolysis of  $\text{SO}_3$ , new sources of SFA formation have received increasing  
54 attention (Zhang et al., 2022; Manonmani et al., 2020, Li et al., 2018, Xue et al., 2024). The  
55 existence of  $\text{HNSO}_2$  was proposed in the reaction between  $\text{SO}_3$  and  $\text{NH}_3$ , and was regarded as the  
56 most stable for nine different isomers of  $\text{HNSO}_2$ , HONSO, HOSNO, HOS(O)N, HSNO<sub>2</sub>, HSONO,  
57 HON(O)S, HOOSN, and HOONS (Deng et al., 2016). Owing to its similarity with  $\text{SO}_3$  and the  
58 potential role of  $\text{SO}_3$  in the atmosphere, the hydrolysis of  $\text{HNSO}_2$  to produce SFA formation has  
59 been focused by several groups (Zhang et al., 2022; Manonmani et al., 2020). As the direct

60 hydrolysis of  $\text{HNSO}_2$  with a high energy barrier takes place hardly in the gas phase (Zhang et al.,  
61 2022; Manonmani et al., 2020), the addition of a second water molecule (Manonmani et al., 2020),  
62 formic acid and sulfuric acid ( $\text{H}_2\text{SO}_4$ , SA) (Zhang et al., 2022) have been proved to promote the  
63 product of SFA through the hydrolysis of  $\text{HNSO}_2$ . It was noted that, with the global reduction in the  
64 concentration of  $\text{H}_2\text{SO}_4$  resulting from  $\text{SO}_2$  emission restrictions, the contribution of  
65 methanesulfonic acid (MSA) to aerosol nucleation has received the widespread attention of  
66 scientists. As a major inorganic acidic air pollutant (Chen et al., 2020), the concentration of MSA  
67 in the atmosphere was noted to be notably high across various regions, spanning from coastal to  
68 continental, with levels found to be between 10% and 250% of those measured for SA (Shen et al.,  
69 2019; Dawson et al., 2012; Bork et al., 2014; Shen et al., 2020; Berresheim et al., 2002; Hu et al.,  
70 2023). However, to the best of our knowledge, the gaseous hydrolysis of  $\text{HNSO}_2$  with MSA has not  
71 yet been investigated, which will confine the understanding for the source of SFA in regions with  
72 significant pollution and high levels of MSA. Thus, understanding the hydrolysis of  $\text{HNSO}_2$  with  
73 MSA in the gas phase was necessary for exploring its impact on aerosols and human health.



75 As a supplement to gas-phase reactions, interfacial reactions at the air-water interface not only  
76 can accelerate the rates of atmospheric reactions but also may introduce new mechanisms (Freeling  
77 et al., 2020; Zhong et al., 2019). For instance, the Criegee intermediates reacting with MSA at the  
78 air-water interface can form the ion pair of  $\text{CH}_3\text{C}(\text{H})(\text{OOH})(\text{SO}_3\text{CH}_3)$  anhydride and  $\text{H}_3\text{O}^+$  (Ma et  
79 al., 2020), which differs from the corresponding gaseous reaction where the MSA molecule acts  
80 solely as a reactant reacting with Criegee intermediates directly. As far as we know,  $\text{HNSO}_2$  exhibit  
81 a significant interfacial preference, as the fact that the total duration time of  $\text{HNSO}_2$  at the interface  
82 approximately accounts for 49.1% of the 150 ns simulation time (Fig. S1). However, the hydrolysis  
83 of  $\text{HNSO}_2$  with MSA has not been studied at the air-water interface, which will limit our  
84 understanding of how the hydrolysis of  $\text{HNSO}_2$  with MSA differs in the gas phase and air-water  
85 interfaces.

86 From a structural point of view, two functional groups of  $-\text{NH}_2$  and  $-\text{SO}_3\text{H}$  in the SFA molecule  
87 can act as both hydrogen donors and acceptors to interact with atmospheric species. Previous studies  
88 have demonstrated that SFA has a potential role in new particle formation (NPF), as it not only  
89 clusters efficiently with itself and SA (Lovejoy and Hanson, 1996), but also can promote the

90 nucleation rate of NPF initiated from SA-DMA by a factor of two in dry and severely contaminated  
91 areas with NH<sub>3</sub> (Li et al., 2018). Due to the concentration of SA in the atmosphere has decreased  
92 significantly with the scenario of SO<sub>2</sub> emission control measures, MSA-driven NPF has attracted  
93 growing attention (Dawson et al., 2012; Nishino et al., 2014; Chen and Finlayson-Pitts, 2017; Chen  
94 et al., 2020; Shen et al., 2020). Initially, the binary nucleation of MSA with inorganic ammonia and  
95 organic amines in the atmosphere has been reported, where MA exhibits the strongest enhancing  
96 capability (Chen et al., 2016; Chen and Finlayson-Pitts, 2017; Shen et al., 2019; Hu et al., 2023).  
97 Subsequently, some reported results suggested that the triadic MSA-MA-driven NPF can exhibit  
98 greater nucleation rates competed to the binary of MSA-driven (Zhang et al., 2022; Hu et al., 2023).  
99 For example, both formic acid (Zhang et al., 2022) and trifluoroacetic acid (Hu et al., 2023) exhibit  
100 an excellent catalytic influence on MSA-MA-driven NPF. However, the SFA involved in MSA-  
101 MA-driven NPF has not been investigated, which is worth important to investigate whether SFA  
102 can exhibit a similar enhancing effect in MSA-MA as observed in SA-DMA.

103 Herein, this work studied the catalytic effect of SFA on H<sub>2</sub>SO<sub>4</sub> hydrolysis and MSA-MA  
104 nucleation particle formation. Specifically, quantum chemical calculations were used firstly to  
105 assess the atmospheric processes of the gaseous hydrolysis of H<sub>2</sub>SO<sub>4</sub> with MSA. Then, the gaseous  
106 and interfacial mechanisms differences of the H<sub>2</sub>SO<sub>4</sub> hydrolysis with MSA were investigated  
107 applying the Born-Oppenheimer Molecular Dynamic (BOMD) simulation method. Finally, the  
108 atmospheric implications and mechanism of SFA in the MSA-MA-dominated NPF process have  
109 been evaluated through density functional theory and the Atmospheric Clusters Dynamic Code  
110 (ACDC) (McGrath et al., 2012; Hu et al., 2023; Zhao et al., 2020; Zhang et al., 2024; Tsona Tchinda  
111 et al., 2022; Liu et al., 2020) models to evaluate the potential effect of SFA on nucleation and NPF.  
112 This work will not only deepen our understanding of the source of SFA, but also reveal significant  
113 implications for new particle formation and aerosol particle growth in MSA polluted areas.

## 114 **2 Methodology**

### 115 **2.1 Quantum Chemical Calculations**

116 The gaseous hydrolysis of H<sub>2</sub>SO<sub>4</sub> with MSA was comprehensively studied through quantum  
117 chemistry simulations. Optimization of all the species were carried out by using the method of M06-  
118 2X with 6-311++G(2df,2pd) basis set (Zhao and Truhlar, 2008; Elm et al., 2012; Bork et al., 2014).

119 Vibrational frequencies were subsequently computed at the M06-2X/6-311++G(2df,2pd) level to  
120 ensure the reality of all stationary point's frequencies and the presence of only one imaginary  
121 frequency in transition states. It is noted that the calculated bond distances and bond angles at the  
122 M06-2X/6-311++G(2df,2pd) level (Fig. S2) agree well with the available values (Fig. S2) from the  
123 experiment and three different theoretical levels of M06-2X/6-311++G(3df,2pd), M062X/6-  
124 311++G(3df,3pd) and M06-2X/aug-cc-pVTZ levels. Also, at the M06-2X/6-311++G(2df,2pd) level,  
125 internal reaction coordinate (IRC) analyses were conducted to verify the connection from the  
126 transition states to the corresponding products (or reactants). All calculations regarding for  
127 geometries and frequency were conducted with the aid of the Gaussian 09 (Frisch, 2009) program.  
128 Furthermore, single point energies were performed at the CCSD(T)-F12/cc-pVDZ-F12 (Kendall et  
129 al., 1992; Adler et al., 2007) level utilizing the ORCA (Neese, 2012) program, based on the  
130 optimized geometries mentioned above. The CCSD(T)/aug-cc-pVDZ method was chosen to  
131 calculate the relative energies as the fact that, compared with unsigned error (Table S1) calculated  
132 at the CCSD(T)/CBS//M06-2X/6-311++G(2df,2pd) level, unsigned errors calculated at CCSD(T)-  
133 F12/cc-pVDZ-F12//M06-2X/6-311++G(2df,2pd) was 0.71 kcal·mol<sup>-1</sup>.

134 **2.2 Rate coefficients calculations**

135 The rate coefficients for the hydrolysis of H<sub>2</sub>SO<sub>3</sub> with MSA were calculated through a two-  
136 step process. Initially, the high-pressure-limit (HPL) rate coefficients were computed applying  
137 VRC-VTST methods within the Polyrate package (Chuang et al., 1999). It's worth noting that the  
138 electronic structure method for VRC-TST calculations is based on Gaussian 09 program using the  
139 M06-2X/6-311++G(2df,2pd). Meanwhile, two pivot points were selected (Bao et al., 2016; Long et  
140 al., 2021; Georgievskii and Klippenstein, 2003; Meana-Pañeda et al., 2024) to produce a single-  
141 faceted dividing surface for the H<sub>2</sub>SO<sub>3</sub> hydrolysis (shown in Part S1 in the Supplement).  
142 Subsequently, on the basis of the HPL rate coefficients, the rate coefficients for the hydrolysis of  
143 H<sub>2</sub>SO<sub>3</sub> with MSA were calculated within the temperature range of 212.6-320.0 K and pressures  
144 applying the Master Equation Solver for Multi-Energy Well Reactions (MESMER) program  
145 (Glowacki et al., 2012). The rate coefficients for the barrierless steps transitioning between reactants  
146 and pre-reactive complexes were assessed applying the Inverse Laplace Transform (ILT) method  
147 within MESMER calculations, while the step transitioning between pre-reactive complexes and  
148 post-reactive complexes via transition states were evaluated using the RRKM theory (Mai et al.,

149 2018) in combination with the asymmetric Eckart model. The details of the rate coefficient for the  
150 hydrolysis of  $\text{HNSO}_2$  without and with  $X$  ( $X = \text{H}_2\text{O}$  and MSA) were given in Part 1, Table 1 and  
151 Table S4.

152 **2.3 BOMD Simulations**

153 BOMD simulations were conducted applying DFT implemented in CP2K program  
154 (Vandevondele et al., 2005; Hutter et al., 2014). The exchange and correlation interactions were  
155 addressed using the Becke-Lee-Yang-Parr (BLYP) functional (Becke, 1988; Lee et al., 1988),  
156 while Grimme's dispersion was applied to address weak dispersion interaction (Grimme et al.,  
157 2010). The Goedecker-Teter-Hutter (GTH) conservation pseudopotential (Goedecker et al.,  
158 1996; Hartwigsen et al., 1998) combine with Gaussian DZVP basis set (Vandevondele and  
159 Hutter, 2007) and an auxiliary plane wave basis set were used to represent core and valence  
160 electrons. Energy cutoffs (Zhong et al., 2017; Zhong et al., 2018; Zhong et al., 2019) of 280 Ry  
161 for the plane wave basis set and 40 Ry for the Gaussian basis set were applied. The gaseous  
162 reactions were simulated in the NVT ensemble at 300 K, with  $15 \times 15 \times 15 \text{ \AA}^3$  supercells and the  
163 time step of 1 fs. To simulate the water microdroplet, the system containing 191 water molecules  
164 (Zhong et al., 2017) was utilized in  $35 \times 35 \times 35 \text{ \AA}^3$  supercells. This setup included  $\text{HNSO}_2$  and  
165 MSA along with the water drop. Prior to the interfacial simulation, a 10 ps relaxation period in  
166 the BOMD simulation was used to equilibrate the water microdroplet system with 191  
167 molecules.

168 **2.4 ACDC kinetics simulation**

169 The ACDC model (McGrath et al., 2012; Hu et al., 2023; Zhao et al., 2020; Zhang et al., 2024;  
170 Tsona Tchinda et al., 2022; Liu et al., 2020) was utilized to simulate the  $(\text{MSA})_x(\text{MA})_y(\text{SFA})_z$  ( $0 \leq y \leq x + z \leq 3$ ) cluster formation rates and explore the potential mechanisms, where the most  
171 stable structure of  $(\text{SFA})_x(\text{MSA})_y(\text{MA})_z$  ( $0 \leq z \leq x + y \leq 3$ ) clusters were searched with  
172 ABCluster software (Zhang and Dolg, 2015) (The details in Part S1 of the Supplement). This  
173 simulation encompasses a variety of temperatures and monomer concentrations to capture the  
174 dynamics under different environmental conditions. Thermodynamic parameters, obtained from  
175 quantum chemical calculations executed at the M06-2X/6-311++G(2df,2pd) level, were used  
176 as inputs for the ACDC model. Notably, many benchmark studies (Zhao et al., 2020; Zhang et al.,  
177 2024; Tsona Tchinda et al., 2022; Liu et al., 2020) show that the M06-2X functional has good

179 performance compared to other common functionals for gaining the Gibbs free energies. For all the  
180 M06-2X calculations with the 6-311++G(2df,2pd) basis set was used, as it is a good compromise  
181 between accuracy and efficiency and does not yield significant errors in the thermal contribution to  
182 the free energy compared to much larger basis sets such as 6-311++G(3df,3pd), with the differences  
183 of relative  $\Delta G$  less than 1.75 kcal·mol<sup>-1</sup> (Table S7). The temporal progression of cluster  
184 concentrations was determined by numerically integrating the birth-death equation, leveraging  
185 MATLAB's ode15s solver for enhanced accuracy.

186 
$$\frac{dc_i}{dt} = \frac{1}{2} \sum_{j < i} \beta_{j,(i-j)} c_j c_{(i-j)} + \sum_j \gamma_{(i+j) \rightarrow i} c_{i+j} - \sum_j \beta_{i,j} c_i c_j - \frac{1}{2} \sum_{j < i} \gamma_{i \rightarrow j} c_i + Q_i - S_i \quad (2)$$

187 Here,  $c_i$  represents the concentration of a specific cluster, labelled as  $i$ ; the term  $\beta_{i,j}$  was used to  
188 denote the collision coefficient, which was a measure of the frequency at which clusters  $i$  and  $j$   
189 collide with each other in a given environment or system; the coefficient  $\gamma_{(i+j) \rightarrow i}$  was defined  
190 as the evaporation rate constant that describes the process of a larger cluster, consisting of  
191 combined elements  $i$  and  $j$ , breaking down into the individual smaller clusters  $i$  and  $j$ ; and  $Q_i$   
192 encompasses all other source terms contributing to the formation of cluster  $i$ .  $S_i$  signifies  
193 alternative sink terms for cluster  $i$  that may remove it from the system. Considering the  
194 formation Gibbs free energy (Table S8) and evaporation rates (Table S9) of all clusters, the  
195 clusters containing pure MSA and MA molecules as well as the clusters containing a SFA  
196 molecule are mostly more stable and therefore are allowed to form larger clusters and contribute  
197 to particle formation rates. In this case, clusters (MSA)<sub>4</sub>·(MA)<sub>3</sub>, (MSA)<sub>4</sub>·(MA)<sub>4</sub> and  
198 SFA·(MSA)<sub>3</sub>·(MA)<sub>3</sub> are set as the boundary clusters.

199 **3. Results and discussions**

200 **3.1 The hydrolysis of H<sub>2</sub>SO<sub>4</sub> with MSA in the gas phase**

201 Given the low chance of three molecules of H<sub>2</sub>SO<sub>4</sub>, H<sub>2</sub>O and MSA colliding simultaneously  
202 under atmospheric conditions, the hydrolysis of H<sub>2</sub>SO<sub>4</sub> with MSA (Channel MSA) was likely a  
203 sequential bimolecular process. As the concentration of water molecule (10<sup>18</sup> molecules·cm<sup>-3</sup>  
204 (Anglada et al., 2013)) in the atmosphere is much higher than those of H<sub>2</sub>SO<sub>4</sub> and MSA (10<sup>5</sup>-10<sup>9</sup>  
205 molecules·cm<sup>-3</sup> (Shen et al., 2020)), the reaction pathway of H<sub>2</sub>SO<sub>4</sub>·MSA + H<sub>2</sub>O is hard to occur  
206 in actual atmospheric conditions. So, Channel MSA proceeds through the initial formation of dimers

207 (HNSO<sub>2</sub>···H<sub>2</sub>O and MSA···H<sub>2</sub>O) via collisions between HNSO<sub>2</sub> (or MSA) and H<sub>2</sub>O. Subsequently,  
208 the generated dimer interacts with the third reactant, either MSA or HNSO<sub>2</sub>. As seen in Fig. 1, the  
209 calculated Gibbs free energy of MSA···H<sub>2</sub>O complex was -0.9 kcal·mol<sup>-1</sup>, which was 4.5 kcal·mol<sup>-1</sup>  
210 lower than that of HNSO<sub>2</sub>···H<sub>2</sub>O. Consequently, it was predicted the primary route for the  
211 hydrolysis reaction of HNSO<sub>2</sub> with MSA takes place via the HNSO<sub>2</sub> + MSA···H<sub>2</sub>O reaction.

212 Starting from the HNSO<sub>2</sub> + MSA···H<sub>2</sub>O reactants, the Channel MSA was initiated through the  
213 intermediate complex designated as IM\_MSA1. From a geometric perspective, IM\_MSA1 complex  
214 exhibits a cage-like configuration by a van der Waals force (S1···O1, 2.00 Å) and the involvement  
215 of three hydrogen bonds of H2···O4 (1.53 Å), H4···N1 (1.60 Å) and H5···O3 (2.07 Å). The Gibbs  
216 free energy of IM\_MSA1 complex relative to HNSO<sub>2</sub> + MSA···H<sub>2</sub>O reactants was 1.7 kcal·mol<sup>-1</sup>.  
217 Subsequently, as presented in Fig. 1, Channel MSA progresses through transition state TS\_MSA1  
218 to yield complex IMF\_MSA1. At TS\_MSA1, the MSA moiety facilitates two hydrogen atom  
219 transfer, with TS\_MSA1 lying only 0.8 kcal·mol<sup>-1</sup> above complex IM\_MSA1. Complex  
220 IMF\_MSA1 exhibits a cage-like structure with a Gibbs free energy was 23.4 kcal·mol<sup>-1</sup> lower than  
221 that of IM\_MSA1, revealing thermodynamic favorability of HNSO<sub>2</sub> hydrolysis with MSA. To  
222 evaluate the relative catalytic impact of MSA and H<sub>2</sub>O, Fig. S4 illustrates the profiles of Gibbs free  
223 energy for the hydrolysis of HNSO<sub>2</sub> and the corresponding reaction assisted by H<sub>2</sub>O. Compared to  
224 complex HNSO<sub>2</sub>···(H<sub>2</sub>O)<sub>2</sub>, the Gibbs stabilization energy of IM\_MSA1 increased by 5.6 kcal·mol<sup>-1</sup>,  
225 potentially shortening the S1···O1 bond distance by 0.21 Å. Considering the Gibbs free energy  
226 barrier and rate coefficients, MSA demonstrates a greater catalytic role compared to H<sub>2</sub>O in  
227 lowering the energy barrier for the hydrolysis of HNSO<sub>2</sub>. In particular, MSA facilitates hydrogen  
228 atom to extraction from H<sub>2</sub>O, further reducing the reaction energy barriers to 7.7 kcal·mol<sup>-1</sup>.  
229 Meanwhile, the calculated rate coefficients for HNSO<sub>2</sub> hydrolysis with MSA was  $3.08 \times 10^{-11}$ - $3.50$   
230  $\times 10^{-11}$  cm<sup>3</sup>·molecule<sup>-1</sup>·s<sup>-1</sup> within 212.6-320.0 K, exceeding corresponding values for reactions  
231 involving H<sub>2</sub>O by 2 orders of magnitude. Besides, the Gibbs free energy of IMF\_MSA1 was 2.0  
232 kcal·mol<sup>-1</sup> lower than that of the product complex IMF\_WM1 (SFA···H<sub>2</sub>O), suggesting SFA has a  
233 higher affinity for MSA compared to H<sub>2</sub>O. Besides, MSA-assisted HNSO<sub>2</sub> hydrolysis is reduced by  
234 4.9 kcal·mol<sup>-1</sup> in energy barrier than the NH<sub>3</sub>-assisted ammonolysis of SO<sub>3</sub> with its rate constant at  
235 298 K ( $2.85 \times 10^{-11}$  cm<sup>3</sup>·molecule<sup>-1</sup>·s<sup>-1</sup>) close to the value of ammonolysis of SO<sub>3</sub> with NH<sub>3</sub> ( $4.35 \times$   
236  $10^{-10}$  cm<sup>3</sup>·molecule<sup>-1</sup>·s<sup>-1</sup>) (Li et al., 2018). However, due to the absence of the concentration of

237 H<sub>2</sub>SO<sub>2</sub>, the competitiveness of these two reactions cannot be further confirmed.

238 To evaluate the comparative catalytic ability of  $X$  ( $X = \text{H}_2\text{O}$  and MSA) in the atmosphere, the  
239 effective rate coefficients ( $k'$ ) for  $X$ -assisted H<sub>2</sub>SO<sub>2</sub> hydrolysis were calculated in Table 1. Notably,  
240  $k'$  serves as a metric for gauging the comparative catalytic ability of a series of gaseous catalysts in  
241 atmospheric reactions (Sarkar et al., 2017; Zhang et al., 2020; Zhang et al., 2019; Buszek et al.,  
242 2012; Gonzalez et al., 2011; Parandaman et al., 2018; Anglada et al., 2013). When  $X$  was present,  
243 the calculated  $k'$  was given by Eq. (3).

$$244 k'_X = k_X \times K_{\text{eq}}(X \cdots \text{H}_2\text{O}) \times [X] \quad (3)$$

245 In Eq. (3),  $k_X$  was the rate coefficient for  $X$ -assisted H<sub>2</sub>SO<sub>2</sub> hydrolysis (Table 1), while  $K_{\text{eq}}(X \cdots \text{H}_2\text{O})$   
246 denotes the equilibrium coefficients of  $X \cdots \text{H}_2\text{O}$  (Table S2).  $[X]$  represents the available  
247 concentrations of H<sub>2</sub>O (Anglada et al., 2013) and MSA (Shen et al., 2020). As indicated in Table 1,  
248 at experimental concentrations ( $[\text{H}_2\text{O}] = 5.16 \times 10^{16} - 2.35 \times 10^{18} \text{ molecules} \cdot \text{cm}^{-3}$ ) within 280.0-320.0  
249 K (at 0 km), the computed  $k'_{\text{WM}}$  ranged from  $5.99 \times 10^{-18} - 7.79 \times 10^{-17} \text{ cm}^3 \cdot \text{molecule}^{-1} \cdot \text{s}^{-1}$ . This range  
250 exceeded  $k'_{\text{MSA}}$  ( $4.60 \times 10^{-21} - 4.81 \times 10^{-20} \text{ cm}^3 \cdot \text{molecule}^{-1} \cdot \text{s}^{-1}$ ) by 2-4 orders of magnitude,  
251 highlighting pronounced impact of H<sub>2</sub>O compared to MSA at 0 km in enhancing the rate of H<sub>2</sub>SO<sub>2</sub>  
252 hydrolysis. However, with the significant decrease in atmospheric water molecules with increasing  
253 altitude, the calculated  $k'_{\text{MSA}}$  ranged from  $1.96 \times 10^{-19} \cdot \text{s}^{-1} - 1.30 \times 10^{-17} \cdot \text{cm}^3 \cdot \text{molecule}^{-1} \cdot \text{s}^{-1}$ ,  
254 surpassing  $k'_{\text{WM}}$  ( $9.85 \times 10^{-27} - 6.51 \times 10^{-22} \cdot \text{cm}^3 \cdot \text{molecule}^{-1} \cdot \text{s}^{-1}$ ) by 3-10 orders of magnitude. This  
255 illustrates that MSA has a significantly greater catalytic ability than H<sub>2</sub>O in accelerating the rate of  
256 H<sub>2</sub>SO<sub>2</sub> hydrolysis within 5-15 km. So, H<sub>2</sub>SO<sub>2</sub> hydrolysis with MSA may represent a potential  
257 formation pathway for SFA across an altitude scope of 5-15 km.

### 258 **3.2 Reactions at the air-water interface**

259 The interfacial mechanism of MSA-assisted H<sub>2</sub>SO<sub>2</sub> hydrolysis at the air-water interface has  
260 not been thoroughly investigated. Interestingly, our simulations show that H<sub>2</sub>SO<sub>2</sub> and MSA  
261 molecules spend approximately 49.1% and 12.1% of the time, respectively, at the air-water interface  
262 during the 150 ns simulation (Fig. S1 and Fig. S6). This reveals that the presence of H<sub>2</sub>SO<sub>2</sub> and  
263 MSA at the air-water interface should not be disregarded. Therefore, BOMD simulations were  
264 performed to clarify the interfacial mechanism of MSA-assisted H<sub>2</sub>SO<sub>2</sub> hydrolysis at the air-water  
265 interface. Comparable to the reactions of SO<sub>3</sub> at the air-water interface with acidic molecules (Cheng  
266 et al., 2023; Zhong et al., 2019a), the hydrolysis of H<sub>2</sub>SO<sub>2</sub> with MSA at the air-water interface may

267 occur through three pathways: (i) the adsorbed MSA interacts with  $\text{HNSO}_2$  at the air-water interface;  
268 (ii) the adsorbed  $\text{HNSO}_2$  interacts with MSA at the air-water interface; and (iii) the  $\text{HNSO}_2\cdots\text{MSA}$   
269 complex reacts at the air-water interface. Nevertheless, because of the high reactivity of MSA at  
270 the air-water interface, the lifetime of MSA was minimal (seen in Fig. S9) on the water droplet,  
271 which was around a small number of picoseconds leading to the rapid formation of  $\text{MSA}^-$  ion.  
272 Meanwhile, although  $\text{HNSO}_2$  remains stable at the air-water interface (seen in Fig. S8) and does not  
273 dissociate within 10 ps, the hydrated form of  $\text{HNSO}_2$  illustrated in Fig. S8 was not conducive to  
274  $\text{HNSO}_2$  hydrolysis at the air-water interface. So, model (iii) was primarily considered for  $\text{HNSO}_2$   
275 hydrolysis with MSA at the air-water interface. It was worth noting that  $\text{HNSO}_2\cdots\text{MSA}$  complex  
276 can persist at the air-water interface for approximately 34.2% of the 150 ns simulation time (see in  
277 Fig. S7). For model (iii), two types of reactions were found at the air-water interface: (a) the  
278  $\text{NH}_2\text{SO}_3^-$  and  $\text{H}_3\text{O}^+$  ions formation mechanism, and (b) the proton exchange mechanism.

279  **$\text{NH}_2\text{SO}_3^-$  and  $\text{H}_3\text{O}^+$  ions forming mechanism.** Fig. 2(a), Fig. S10 and Movie 1 illustrates the  
280 formation mechanism of  $\text{NH}_2\text{SO}_3^-$  and  $\text{H}_3\text{O}^+$  ions through the chain structure. At 4.57 ps, a chain  
281 hydrolyzed transition state was observed, accompanied by two protons transfer events. Specially,  
282 an H2 atom transferred from the OH moiety of MSA molecule to the terminal N atom of  $\text{HNSO}_2$   
283 molecule, resulting in the breaking of the O3-H2 bond (with the length of 1.49 Å) and forming the  
284 H2-N bond (with the length of 1.14 Å). Concurrently, an interfacial water molecule decomposes,  
285 leading to the elongation of the O1-H1 bond to over 1.00 Å, with the S1 atom of  $\text{HNSO}_2$  obtaining  
286 the OH moiety of the interfacial water molecule ( $d_{(\text{S1-O1})} = 1.60$  Å). By 4.61 ps, The N-H2 and S1-  
287 O1 bonds both shortened to 0.99 Å and 1.01 Å, revealing the formation of the SFA molecule.  
288 However, due to its strong acidity, the SFA molecule could only persist on the water droplet surface  
289 for a ps time-scale. As a result, at 7.43 ps, the proton of SFA transferred to another interfacial water  
290 molecule, completing the deprotonation of SFA. The loop structure mechanism (Fig. 2(b), Fig. S11  
291 and Movie 2) was similar with the chain structure mechanism. However, in this case, the proton of  
292 SFA transferred to  $\text{CH}_3\text{SO}_3^-$  rather than to an interfacial water molecule.

293 **Proton exchange mechanism.** As depicted in Fig. 3, the proton exchange mechanism  
294 illustrates the deprotonation of MSA concurrent with  $\text{HNSO}_2$  hydration at the air-water interface.  
295 As shown in Fig. 3(a), Fig. S12 and Movie 3, MSA-mediated hydration  $\text{HNSO}_2$  with a single water  
296 molecule was observed. Initially, the  $\text{HNSO}_2\cdots\text{MSA}$  complex quickly associates with an interfacial

water molecule, and forms a loop structure complex that accelerates the rate of proton transfer. By 4.38 ps, an eight-membered loop structure complex,  $\text{HNSO}_2\cdots\text{H}_2\text{O}\cdots\text{MSA}$ , emerges, characterized by two hydrogen bonds ( $d_{(\text{H}_2\text{-N})} = 1.82 \text{ \AA}$  and  $d_{(\text{H}_1\text{-O}_2)} = 1.92 \text{ \AA}$ ) and a van der Waals forces ( $d_{(\text{S1-O1})} = 2.35 \text{ \AA}$ ). Thereafter, at 4.77 ps, a transition state-like configuration was identified where the water molecule within the loop complex dissociated, elongating the O1-H1 bond to over 1.00  $\text{\AA}$ , and the S atom of  $\text{HNSO}_2$  attaches to the OH group of the interfacial water molecule. Concurrently, the  $\text{CH}_3\text{SO}_3^-$  ion receives the proton from the separated interfacial water molecule. The entire reaction for MSA-mediated hydration  $\text{HNSO}_2$  with one water molecule was completed at 4.80 ps, resulting in the formation of SFA and MSA molecules. MSA-mediated hydration of  $\text{HNSO}_2$  with two water molecules (Fig. 3(b), Fig. S13 and Movie 4) at the air-water interface was similar with mechanism identified with one water molecule. However, the inclusion of two water molecules enlarges the loop, significantly reducing the stress on the loop structures. Consistent with the prediction in Fig. 4, the loop structures preferred to include two water molecules rather than one water molecule. This observation agrees well with the reported hydration of Criegee intermediate at the air-water interface (Zhu et al., 2016; Kumar et al., 2018; Liu et al., 2021; Zhang et al., 2023a). Additionally, MSA-mediated hydration of  $\text{HNSO}_2$  with three water molecules (Fig. S14 and Movie 5) has been observed in the proton exchange mechanism. However, its probability of occurrence was smaller due to the relatively larger entropy effect. It was noteworthy that the SFA and MSA molecules formed in the proton exchange mechanism were not stable at the air-water interface, which can further interact with an interfacial water molecule to form the corresponding ions of  $\text{NH}_2\text{SO}_3^-$  and  $\text{CH}_3\text{SO}_3^-$ .

At the air-water interface, a sum of 50 BOMD trajectories, each lasting 10 ps, were conducted to investigate  $\text{HNSO}_2$  hydrolysis with MSA. Two distinct mechanisms were observed: the formation of  $\text{NH}_2\text{SO}_3^-$  and  $\text{H}_3\text{O}^+$  ions formation (shown in blue and yellow in Fig. 4) and the proton exchange mechanism (represented by orange, purple and green in Fig. 4). In the mechanism involving the formation of  $\text{NH}_2\text{SO}_3^-$  and  $\text{H}_3\text{O}^+$  ions, approximately 22% (Fig. 2(a), Fig. 4, Fig. S10 and Movie 1) of the reactions took place via a chain structure, while the majority (~18%) (Fig. 2(b), Fig. 4, Fig. S11 and Movie 2) proceeded through a loop structure mechanism. This discrepancy can be attributed to the uncertainty regarding the direction of proton transfer from SFA. Since the number of water molecules near the water microdroplet far exceeded that of  $\text{CH}_3\text{SO}_3^-$ , protons were predominantly transferred to interface water molecules, making the loop structure mechanism weaker than the

327 chain structure mechanism. Approximately 60% of the reactions were observed to be due to the  
328 proton exchange mechanism in BOMD simulations. Through water-mediated mechanisms, these  
329 reactions resulted in SFA formation. Similarly to gas-phase reactions, loop structures were observed  
330 in these reactions. Approximately 10% of the reactions formed a loop structure involving one water  
331 molecule (Fig. 3(a), Fig. 4, Fig. S12 and Movie 3), while the most common loop structure involved  
332 two water molecules (about 42%) (Fig. 3(b), Fig. 4, Fig. S13 and Movie 4). Smaller loops were  
333 found to experience more stress than loop structures with two water molecules. In cases of loop  
334 structures with three water molecules (about 8%) (Fig. 4, Fig. S14 and Movie 5), the entropy effect  
335 was deemed to be more significant than the strain effect and likely played a dominant role. The two  
336 water molecules contained in the loop structure not only acted as a reactant but also facilitated proton  
337 transfer as a bridge.

338 **3.3 New Particle Formation from the atmospheric products**

339 **3.3.1. The influence of SFA on the stability of atmospheric MSA-MA-based  
340 clusters**

341 Electrostatic Potential (ESP) mapping on the molecular van der Waals (vdW) surface was  
342 employed to analyze the interactions between SFA and other key nucleation precursors like MSA  
343 and MA. As shown in Fig. 5, sites with more negative ESP often attract more positive ESP sites,  
344 namely hydrogen bonds in the studied system. Specifically, the hydrogen atoms of the -SO<sub>3</sub>H and -  
345 NH<sub>2</sub> groups (site 4 and 5) in SFA, possessing more positive ESP values, have the potential to attract  
346 groups with negative ESP values, such as the oxygen atom within the -SO<sub>3</sub>H group of MSA (site 6)  
347 and the nitrogen atom of MA (site 1), thus forming hydrogen bonds as proton donors. Additionally,  
348 the sulfur atom of the -SO<sub>3</sub>H functional group (site 7) in SFA, with a negative ESP of -30.75, acts  
349 as proton acceptor, facilitating direct binding with MSA and MA molecules via the hydrogen bonds.  
350 Therefore, the introduction of SFA was believed to enhance the stability of MSA-MA clusters by  
351 promoting the formation of more hydrogen bonds and facilitating proton transfers.

352 **3.3.2. The cluster formation rates in the SFA-MSA-MA system**

353 Simulations were conducted to determine the cluster formation rates ( $J$ ) for the MSA-MA-SFA  
354 system, varying parameters such as temperature and the concentrations of the precursors were  
355 involved. To assess the promotional impact of SFA on  $J$  under varying atmospheric conditions, the  
356 enhancement factor ( $R$ ) was computed as the ratio of  $J_{MSA-MA-SFA}$  to  $J_{MSA-MA}$ . As depicted in Fig. 6

357 (a), the  $J$  of MSA-MA-SFA system exhibits a negative correlation with temperature, attributed to  
358 the decrease in  $\Delta G$  value and evaporation rates of clusters at lower temperatures. Conversely, a  
359 positive correlation of  $R$  with temperature was observed (Fig. 6(b)), indicating that SFA's  
360 enhancement of nucleation was more pronounced in regions with relatively higher temperatures.  
361 Furthermore, both  $J$  and  $R$  show an increase as the [SFA] increases, suggesting a positive correlation  
362 of  $J$  and  $R$  with [SFA]. In short, in regions with high [SFA], such as the Yangtze River Delta of  
363 China, Bangladesh, and the east coast of India, SFA was expected to significantly boost the  $J$  of  
364 MSA-MA based nucleation. It is noted that in Fig. 6(b), due to the competitive relationship between  
365 MSA and SFA, at low concentrations of SFA, the binding capacity of MSA with MA is stronger  
366 than that of SFA with MA, resulting in only a small amount of SFA participating in cluster formation.  
367 However, as the concentration of SFA increases, the number of  $(MSA)_x \cdot (MA)_y \cdot (SFA)_z$  (where  $y \leq$   
368  $x + z \leq 3$ ) ternary clusters increase, leading to the formation of more hydrogen bonds and a  
369 significant increase in  $R_{SFA}$ . Additionally, Fig. 7 illustrates the  $J$  and  $R$  of MSA-MA-SFA clusters  
370 under different [MSA] and [MA]. On one hand, larger values of [MSA] and [MA] correspond to  
371 higher  $J$ , as the increased concentration of nucleation precursors leads to a rise in the number of  
372 MSA-MA-FSA clusters. On the other hand, increasing [MSA] and [MA] result in a decrease in the  
373  $R$  attributed to the effect of SFA on nucleation. This was because as [MSA] and [MA] increases,  
374 the prevalence of pure MSA-MA clusters rise during the clustering process, consequently reducing  
375 the impact of SFA.

### 376 **3.3.3. The growth paths of cluster under different atmospheric conditions**

377 Li et al. studied the atmospheric concentration of SFA estimated by theoretical method (Li et  
378 al., 2018) was expected to reach up to  $10^8$  molecules· $\text{cm}^{-3}$  in high  $\text{NH}_3$  concentrations, such as  
379 Yangtze River Delta in China (Yu et al., 2020), Indo-Gangetic Plains (Kuttippurath et al., 2020),  
380 Pakistan, Bangla desh (Warner et al., 2016), and the southern Italy (Tang et al., 2021). Considering  
381 the high-atmospheric concentrations of MSA and MA detected in coastal industrial areas (Stieger  
382 et al., 2021; Mochizuki et al., 2017;), SFA could be an important contributor to MSA-MA-driven  
383 NPF, such as the Yangtze River Delta in China, the east coast of India, the south of Bangladesh and  
384 Italy. To further evaluate the implication of SFA for the MSA-MA nucleation in the atmosphere,  
385 the growth paths of cluster was calculated under different atmospheric conditions. In Fig. 8 (a), two  
386 main types of cluster formation routes were found: (i) the pure MSA-MA pathway and (ii) the MSA-

387 MA-SFA pathways at 278.15 K in the studied system. In the pure MSA-MA pathway, cluster  
388 growth primarily occurs through the collisional addition of MSA or MA monomers. Conversely, in  
389 the SFA-involved pathways, SFA can directly participate in the formation of stable larger clusters  
390 subsequently, such as  $(MSA)_2 \cdot (MA)_2 \cdot SFA$  and  $(MSA)_2 \cdot (MA)_2 \cdot (SFA)_2$  clusters, and then  
391 subsequently grow out. The involvement of SFA in the cluster formation pathway was significantly  
392 influenced by atmospheric conditions. Firstly, as the temperature rises from 238.15 K to 278.15 K,  
393 the contribution of the SFA-involved cluster formation pathways rises from 68% to 90% (Fig. 8  
394 (b)), implying that the pathway involving SFA becomes increasingly important at lower altitudes or  
395 in warmer conditions. Secondly, as depicted in Fig. 8(c) and Fig. S22, the contribution of SFA to  
396 the MSA-MA system is primarily influenced by [SFA] and [MSA], with negligible dependence on  
397 [MA]. To assess the role of SFA in MSA-MA nucleation in the atmosphere, the specific contribution  
398 of the MSA-MA cluster growth paths at varying [SFA] to NPF was calculated at 278.15 K, as  
399 illustrated in Fig. 8(c), under the ambient conditions typical of the corresponding regions. Generally,  
400 as [SFA] increases from  $10^4$  to  $10^8$  molecules·cm<sup>-3</sup>, the contribution of the SFA-involved pathway  
401 increases gradually. Specifically, at low [SFA] ( $10^4$  molecules·cm<sup>-3</sup>), the contributions of SFA-  
402 involved clustering pathways are 77% and 41% in regions with relatively low [MSA] in non-sea  
403 regions (Berresheim et al., 2002). In regions with high [SFA] ( $10^6$ ,  $10^8$  molecules·cm<sup>-3</sup>), the  
404 contributions of the SFA-MSA-MA growth pathways are dominant in their NPF. Particularly in  
405 areas with high [MSA], such as the Pacific Rim ( $6.26 \times 10^8$  molecules·cm<sup>-3</sup> (Saltzman et al., 1986)),  
406 the central Mediterranean Sea ( $2.11 \times 10^8$  molecules·cm<sup>-3</sup> (Mansour et al., 2020)) and the Amundsen  
407 Sea ( $3.65 \times 10^9$  molecules·cm<sup>-3</sup> (Jung et al., 2020)), nucleation is primarily driven by the SFA-  
408 MSA-MA pathway, contributing to approximately 88% of cluster formation. These results suggest  
409 that the influence of SFA is more pronounced in regions with relatively high [MSA]. It is important  
410 to note that the [SFA] values discussed in this work are estimated from limited observational data  
411 based on the reaction between  $SO_3$  and  $NH_3$  in the atmosphere. Accurate determination of  
412 atmospheric [SFA] requires extensive field observations to enable more comprehensive research.

#### 413 **3.4 Interfacial implications of products on aerosol particle growth**

414 As the discussion above, the formation of  $SFA^- \cdots H_3O^+$  and  $MSA^- \cdots H_3O^+$  ions pairs can occur  
415 within a few picoseconds at the air-water interface. The atmospheric affinity of  $MSA^-$ ,  $SFA^-$  and  
416  $H_3O^+$  for gaseous precursors was further probed by evaluating the free energies of interaction. It

417 was worth noting that compounds such as MSA, MA, HNO<sub>3</sub> (NA), and (COOH)<sub>2</sub> (OA) were  
418 identified as candidate species for consideration (Wang et al., 2024; Kulmala et al., 2004). As  
419 presented in Table 2, the computed binding energies demonstrate that the interactions of SFA<sup>-</sup>  
420  $\cdots$ MSA, SFA<sup>-</sup> $\cdots$ NA, SFA<sup>-</sup> $\cdots$ OA, H<sub>3</sub>O<sup>+</sup> $\cdots$ MA, MSA<sup>-</sup> $\cdots$ MSA, MSA<sup>-</sup> $\cdots$ OA, and MSA<sup>-</sup> $\cdots$ NA were  
421 stronger than those of MSA $\cdots$ MA (one of the primary precursors for atmospheric aerosols), with  
422 their Gibbs free energies increased by 14.3-50.9 kcal $\cdot$ mol<sup>-1</sup>. The findings indicate that the presence  
423 of SFA<sup>-</sup>, MSA<sup>-</sup>, and H<sub>3</sub>O<sup>+</sup> at the interface facilitates the capture of potential gaseous species onto  
424 the surface of water microdroplet.

425 Furthermore, we investigated the possibility of SFA<sup>-</sup> contributing to the enlargement of  
426 particles within the MSA-MA cluster, taking into account the geometric configuration and the free  
427 energy of formation for the (MSA)<sub>1</sub> $\cdot$ (MA)<sub>1</sub> $\cdot$ (SFA<sup>-</sup>)<sub>1</sub> clusters aggregating. Compared with other  
428 clusters, such as (MSA)<sub>1</sub> $\cdot$ (MA)<sub>1</sub> $\cdot$ (X)<sub>1</sub> (where X = HCOOH, CH<sub>3</sub>COOH, CHOCOOH, OA,  
429 CH<sub>3</sub>COCOOH, HOOCCH<sub>2</sub>COOH, HOOC(CH)<sub>2</sub>COOH, HOOC(CH<sub>2</sub>)<sub>2</sub>COOH,  
430 HOOC(CH<sub>2</sub>)<sub>3</sub>COOH, C<sub>6</sub>H<sub>5</sub>(COOH) and C<sub>10</sub>H<sub>16</sub>O<sub>3</sub>) clusters (Zhang et al, 2022), the quantity of  
431 hydrogen bonds within the (MSA)<sub>1</sub> $\cdot$ (MA)<sub>1</sub> $\cdot$ (SFA<sup>-</sup>)<sub>1</sub> cluster has increased, and the loop of complex  
432 was expanded. It has been demonstrated that SFA<sup>-</sup> has the greatest capacity to stabilize MSA-MA  
433 clusters and facilitate MSA-MA nucleation in these clusters. This was attributed to its acidic nature  
434 and structural characteristics, which include a greater number of intermolecular hydrogen bond  
435 binding sites. Therefore, relative to (MSA)<sub>1</sub> $\cdot$ (MA)<sub>1</sub> $\cdot$ (X)<sub>1</sub> cluster (Table 2), the Gibbs formation free  
436 energy  $\Delta G$  of the (MSA)<sub>1</sub> $\cdot$ (MA)<sub>1</sub> $\cdot$ (SFA<sup>-</sup>)<sub>1</sub> cluster was lower, indicating that the NH<sub>2</sub>SO<sub>3</sub><sup>-</sup> ion  
437 exhibits a more potent nucleation capacity at the air-water interface compared to the X species in  
438 the gas phase. Consequently, our forecast was that the presence of NH<sub>2</sub>SO<sub>3</sub><sup>-</sup> at the air-water interface  
439 will foster enhanced particle growth.

440 **4. Summary and Conclusions**

441 In this study, quantum chemical calculations, BOMD simulations and ACDC kinetic model  
442 were utilized to characterize the gaseous and interfacial hydrolysis of HNSO<sub>2</sub> with MSA, and to  
443 examine the influence exerted by SFA on MSA-MA-based clusters.

444 In the gaseous reaction, the activation energy for the hydrolysis of HNSO<sub>2</sub> catalyzed by MSA  
445 was only 0.8 kcal $\cdot$ mol<sup>-1</sup>, significantly lower by 7.7 kcal $\cdot$ mol<sup>-1</sup> than the energy barrier of H<sub>2</sub>O-assisted

446 HNSO<sub>2</sub> hydrolysis. The effective rate coefficients reveal that the SFA formation from MSA-  
447 catalyzed hydrolysis of HNSO<sub>2</sub> can be competitive with that catalyzed by H<sub>2</sub>O within an altitude of  
448 5-15 km. Moreover, kinetic simulations utilizing the ACDC have disclosed that SFA has an  
449 unexpectedly positive impact on the NPF process, markedly enhancing the assembly of MSA-MA-  
450 based cluster. Notably, the “participant” mechanism of SFA for cluster formation has been identified  
451 by tracing the growth paths of the system in agriculture-developed and coastal industrial areas,  
452 especially significant in the Yangtze River Delta of China, Bangladesh, and the east coast of India.

453 At the air-water interface, the NH<sub>2</sub>SO<sub>3</sub><sup>-</sup> and H<sub>3</sub>O<sup>+</sup> ions forming mechanism (~40%) and the  
454 proton exchange mechanism (~60%) were observed in the hydrolysis of HNSO<sub>2</sub> with MSA, which  
455 can take place in a few picoseconds. Notably, the formed SFA<sup>-</sup>, MSA<sup>-</sup>, and H<sub>3</sub>O<sup>+</sup> ions at the air-  
456 water interface possess the ability to attract potential precursor molecules like MSA, MA, and  
457 HNO<sub>3</sub>. This attraction facilitates the transition of gaseous molecules onto the surface of water  
458 microdroplet. Moreover, the assessment of the potential of *X* in the formation of the ternary MSA-  
459 MA-*X* cluster revealed that SFA<sup>-</sup> exhibits the greatest propensity to stabilize MSA-MA clusters and  
460 to foster nucleation of MSA-MA in the context of *X*.

461 Overall, this work not only elucidates a novel mechanism underlying the hydrolysis of HNSO<sub>2</sub>  
462 with MSA, but also highlight the potential contribution of SFA on aerosol particle growth and new  
463 particle formation.

#### 464 **Data availability.**

465 All data presented in this study are available upon request from the corresponding author.

#### 466 **Author contributions.**

467 HW: methodology, validation, investigation, writing (original draft). SW: writing (review),  
468 conceptualization, methodology, investigation. JY: writing (review), data computation. YY: data  
469 curation, data computation. RL: writing (editing), data curation, visualization, investigation. RW:  
470 data curation, formal analysis, funding acquisition. CZ: data curation, project administration,  
471 writing (review and editing). TZ: methodology, formal analysis, funding acquisition. CZ: writing  
472 (review and editing), formal analysis.

#### 473 **Competing interests.**

474 The authors declare that they have no known competing financial interests or personal  
475 relationships that could have appeared to influence the work reported in this paper.

476 **Acknowledgments.**

477 This work was supported by the National Natural Science Foundation of China (No: 22073059;  
478 22203052); the Key Cultivation Project of Shaanxi University of Technology (No: SLG2101); the  
479 Education Department of Shaanxi Provincial Government (No. 23JC023).

480 **Financial support.**

481 This research has also been supported by the Education Department of Shaanxi Provincial  
482 Government (No. 23JC023).

483

## 484 Reference

485 Adler, T. B., Knizia, G., and Werner, H. J.: A simple and efficient CCSD(T)-F12 approximation, *J. Chem.*  
486 *Phys.*, 127, 22, 2007.

487 Anglada, J. M., Hoffman, G. J., Slipchenko, L. V. M., Costa, M., Ruiz-Lopez, M. F., and Francisco, J. S.:  
488 Atmospheric significance of water clusters and ozone-water complexes, *J. Phys. Chem. A*, 117, 10381-  
489 10396, 2013.

490 Bao, J. L., Zhang, X., and Truhlar, D. G.: Barrierless association of  $\text{CF}_2$  and dissociation of  $\text{C}_2\text{F}_4$  by  
491 variational transition-state theory and system-specific quantum Rice-Ramsperger-Kassel theory, *Proc.*  
492 *Natl. Acad. Sci. USA.*, 113, 13606-13611, 2016.

493 Becke, A. D.: Density-functional exchange-energy approximation with correct asymptotic behavior,  
494 *Phys. Rev. A.*, 38, 3098-3100, 1988.

495 Berresheim, H., Elste, T., Tremmel, H. G., Allen, A. G., Hansson, H. C., Rosman, K., Dal Maso, M.,  
496 Mäkelä, J. M., Kulmala, M., and O'Dowd, C. D.: Gas-aerosol relationships of  $\text{H}_2\text{SO}_4$ , MSA, and OH:  
497 Observations in the coastal marine boundary layer at Mace Head, Ireland, *J. Geophys. Res. Atmos.*, 107,  
498 PAR 5-1-PAR 5-12, 2002.

499 Bork, N., Elm, J., Olenius, T., and Vehkamäki, H.: Methane sulfonic acid-enhanced formation of  
500 molecular clusters of sulfuric acid and dimethyl amine, *Atmos. Chem. Phys.*, 14, 12023-12030, 2014.

501 Bork, N., Du, L., Reiman, H., Kurten, T., and Kjaergaard, H. G.: Benchmarking ab initio binding energies  
502 of hydrogen-bonded molecular clusters based on FTIR spectroscopy, *J. Phys. Chem. A*, 118, 5316-5322,  
503 2014.

504 Buszek, R. J., Torrent-Sucarrat, M., Anglada, J. M., and Francisco, J. S.: Effects of a single water  
505 molecule on the  $\text{OH} + \text{H}_2\text{O}_2$  reaction, *J. Phys. Chem. A*, 116, 5821-5829, 2012.

506 Chen, D., Li, D., Wang, C., Luo, Y., Liu, F., and Wang, W.: Atmospheric implications of hydration on the  
507 formation of methanesulfonic acid and methylamine clusters: A theoretical study, *Chemosphere.*, 244,  
508 125538-125547, 2020.

509 Chen, H. and Finlayson-Pitts, B. J.: New particle formation from methanesulfonic acid and  
510 amines/ammonia as a function of temperature, *Environ. Sci. Technol.*, 51, 243-252, 2017.

511 Chen, H., Varner, M. E., Gerber, R. B., Finlayson-Pitts, B. J., Reactions of methanesulfonic acid with  
512 amines and ammonia as a source of new particles in air. *J. Phys. Chem. B* 2016, 120, 1526-1536.

513 Cheng, Y., Ding, C., Wang, H., Zhang, T., Wang, R., Muthiah, B., Xu, H., Zhang, Q., and Jiang, M.:  
514 Significant influence of water molecules on the  $\text{SO}_3 + \text{HCl}$  reaction in the gas phase and at the air-water  
515 interface, *Phys. Chem. Chem. Phys.*, 25, 28885-28894, 2023.

516 Chuang, Y., Corchado, J., Fast, P., Villa, J., Coitino, E., Hu, W., Liu, Y., Lynch, G., Nguyen, K., and  
517 Jackels, C.: Polyrate-version 8.2, University of Minnesota, Minneapolis, 1999.

518 Dawson, M. L., Varner, M. E., Perraud, V., Ezell, M. J., Gerber, R. B., and Finlayson-Pitts, B. J.:  
519 Simplified mechanism for new particle formation from methanesulfonic acid, amines, and water via  
520 experiments and ab initio calculations, *Proc. Natl. Acad. Sci. USA.*, 109, 18719-18724, 2012.

521 Dawson, M. L., Varner, M. E., Perraud, V. M., Ezell, M. J., Wilson, J. M., Zelenyuk, A., Gerber, R. B.,  
522 and Finlayson-Pitts, B. J.: Amine-amine exchange in aminium-methanesulfonate aerosols, *J. Phys. Chem.*  
523 C., 118(50):29431-29440, 2014.

524 Deng, G., Wu, Z., Li, D., Linguerri, R., Francisco, J. S., and Zeng, X. J. J. o. t. A. C. S.: Simplest N-  
525 Sulfonylamine  $\text{HNSO}_2$ , *J. Am. Chem. Soc.*, 140, 138, 11509-11512, 2016.

526 Ding, C., Cheng, Y., Wang, H., Yang, J., Li, Z., Lily, M., Wang, R., and Zhang, T.: Determination of the

527 influence of water on the  $\text{SO}_3 + \text{CH}_3\text{OH}$  reaction in the gas phase and at the air-water interface, *Phys.*  
528 *Chem. Chem. Phys.*, 25, 15693-15701, 2023.

529 Elm, J.: Clusteromics II: methanesulfonic acid-base cluster formation, *ACS omega.*, 6, 17035-17044,  
530 2021.

531 Elm, J., Bilde, M., and Mikkelsen, K. V.: Assessment of density functional theory in predicting structures  
532 and free energies of reaction of atmospheric prenucleation clusters, *J. Chem. Theory Comput.*, 8, 2071-  
533 2077, 2012.

534 Freeling, F., Scheurer, M., Sandholzer, A., Armbruster, D., Nödler, K., Schulz, M., Ternes, T. A., and  
535 Wick, A.: Under the radar – Exceptionally high environmental concentrations of the high production  
536 volume chemical sulfamic acid in the urban water cycle, *Water Research.*, 175, 115706, 2020.

537 Frisch, M. J., Trucks, G. W., Schlegel, H. B., Scuseria, G. E., Robb, M. A., Cheeseman, J. R., Scalmani,  
538 G., Barone, V., Mennucci, B., Petersson, G. A., Nakatsuji, H., Caricato, M., Li, X., Hratchian, H. P.,  
539 Izmaylov, A. F., Bloino, J., Zheng, G., Sonnenberg, J. L., Hada, M., Ehara, M., Toyota, K., Fukuda, R.,  
540 Hasegawa, J., Ishida, M., Nakajima, T., Honda, Y., Kitao, O., Nakai, H., Vreven, T., Montgomery, J. A.  
541 Jr., Peralta, J. E., Ogliaro, F., Bearpark, M., Heyd, J. J., Brothers, E., Kudin, K. N., Staroverov, V. N.,  
542 Kobayashi, R., Normand, J., Raghavachari, K., Rendell, A., Burant, J. C., Iyengar, S. S., Tomasi, J., Cossi,  
543 M., Rega, N., Millam, J. M., Klene, M., Knox, J. E., Cross, J. B., Bakken, V., Adamo, C., Jaramillo, J.,  
544 Gomperts, R., Stratmann, R. E., Yazyev, O., Austin, A. J., Cammi, R., Pomelli, C., Ochterski, J. W.,  
545 Martin, R. L., Morokuma, K., Zakrzewski, V. G., Voth, G. A., Salvador, P., Dannenberg, J. J., Dapprich,  
546 S., Daniels, A. D., Farkas, Ö., Foresman, J. B., Ortiz, J. V., Cioslowski, J., and Fox, D. J.: Gaussian09  
547 Revision D. 01, Gaussian Inc. Wallingford CT, Gaussian Inc. Wallingford CT, See also: URL: <http://www.gaussian.com>, 2009.

548 Georgievskii, Y. and Klippenstein, S.: Variable reaction coordinate transition state theory: analytic results  
549 and application to the  $\text{C}_2\text{H}_3 + \text{H} \rightarrow \text{C}_2\text{H}_4$  reaction, *JCP*, 118, 5442-5455, 2003.

550 Glowacki, D. R., Liang, C.-H., Morley, C., Pilling, M. J., and Robertson, S. H.: MESMER: an open-  
551 source master equation solver for multi-energy well reactions, *J. Phys. Chem. A*, 116, 9545-9560, 2012.

552 Goedecker, S., Teter, M., and Hutter, J.: Separable dual-space Gaussian pseudopotentials, *Phys. Rev. B.*,  
553 54, 1703, 1996.

554 Gonzalez, J., Anglada, J. M., Buszek, R. J., and Francisco, J. S.: Impact of water on the  $\text{OH} + \text{HOCl}$   
555 reaction, *J. Am. Chem. Soc.*, 133, 3345-3353, 2011.

556 Grimme, S., Antony, J., Ehrlich, S., and Krieg, H.: A consistent and accurate ab initio parametrization of  
557 density functional dispersion correction (DFT-D) for the 94 elements H-Pu, *J. Chem. Phys.*, 132, 154104,  
558 2010.

559 Hartwigsen, C., Goedecker, S., and Hutter, J.: Relativistic separable dual-space Gaussian  
560 pseudopotentials from H to Rn, *Phys. Rev. B.*, 58, 3641-3662, 1998.

561 Hirota, K., Mäkelä, J., and Tokunaga, O.: Reactions of sulfur dioxide with ammonia: Dependence on  
562 oxygen and nitric oxide, *Ind. Eng. Chem. Res.*, 35, 3362-3368, 1996.

563 Hu, Y., Chen, S., Ye, S., Wei, S., Chu, B., Wang, R., Li, H., and Zhang, T.: The role of trifluoroacetic acid  
564 in new particle formation from methanesulfonic acid-methylamine, *Atmos. Environ.*, 311, 120001, 2023.

565 Hutter, J., Iannuzzi, M., Schiffmann, F., and VandeVondele, J.: Cp2k: atomistic simulations of condensed  
566 matter systems, *WIREs COMPUT MOL SCI.*, 4, 15-25, 2014.

567 Jung, J., Hong, S. B., Chen, M., Hur, J., Jiao, L., Lee, Y., Park, K., Hahm, D., Choi, J. O., Yang, E. J.,  
568 and Physics: Characteristics of methanesulfonic acid, non-sea-salt sulfate and organic carbon aerosols  
569 over the Amundsen Sea, Antarctica, *Atmos. Chem. Phys.*, 20, 5405-5424, 2020.

570

571 Kendall, R. A., T. H. D., and Harrison, R. J.: Electron affinities of the first-row atoms revisited.  
572 Systematic basis sets and wave functions, *J. Chem. Phys.*, 96, 6796-6806, 1992.

573 Kim, T. O., Ishida, T., Adachi, M., Okuyama, K., and Seinfeld, J. H.: Nanometer-sized particle formation  
574 from  $\text{NH}_3/\text{SO}_2/\text{H}_2\text{O}/\text{air}$  mixtures by ionizing irradiation, *Aerosol Sci. Tech.*, 29, 111-125, 1998.

575 Kolb, C., Jayne, J., Worsnop, D., Molina, M., Meads, R., and Viggiano, A.: Gas phase reaction of sulfur  
576 trioxide with water vapor, *J. Am. Chem. Soc.*, 116, 10314-10315, 1994.

577 Kulmala, M., Vehkämäki, H., Petäjä, T., Dal Maso, M., Lauri, A., Kerminen, V. M., Birmili, W., and  
578 McMurry, P. H.: Formation and growth rates of ultrafine atmospheric particles: a review of observations,  
579 *J. Aerosol Sci.*, 35, 143-176, 2004.

580 Kumar, M., Li, H., Zhang, X., Zeng, X. C., and Francisco, J. S.: Nitric acid-amine chemistry in the gas  
581 phase and at the air-water interface, *J. Am. Chem. Soc.*, 140, 6456-6466, 2018.

582 Kuttippurath, J., Singh, A., Dash, S., Mallick, N., Clerbaux, C., Van Damme, M., Clarisse, L., Coheur,  
583 P.-F., Raj, S., and Abbhishek, K.: Record high levels of atmospheric ammonia over India: Spatial and  
584 temporal analyses, *Sci. Total Environ.*, 740, 139986, 2020.

585 Larson, L. J. and Tao, F.-M.: Interactions and reactions of sulfur trioxide, water, and ammonia: An ab  
586 initio and density functional theory study, *J. Phys. Chem. A*, 105, 4344-4350, 2001.

587 Lee, C., Yang, W., and Parr, R. G.: Development of the colle-Salvetti correlation-energy formula into a  
588 functional of the electron density, *PHYS REV B*, 37, 785, 1988.

589 Li, H., Zhong, J., Vehkämäki, H., Kurtén, T., Wang, W., Ge, M., Zhang, S., Li, Z., Zhang, X., Francisco,  
590 J. S., and Zeng, X. C.: Self-Catalytic reaction of  $\text{SO}_3$  and  $\text{NH}_3$  to produce sulfamic acid and its implication  
591 to atmospheric particle formation, *J. Am. Chem. Soc.*, 140, 11020-11028, 2018.

592 Liu, J., Liu, Y., Yang, J., Zeng, X. C., and He, X.: Directional proton transfer in the reaction of the simplest  
593 criegee intermediate with water involving the formation of transient  $\text{H}_3\text{O}^+$ , *J. Phys. Chem. Lett.*, 12,  
594 3379-3386, <https://doi.org/10.1021/acs.jpclett.1c00448>, 2021.

595 Liu, L., Yu, F., Tu, K., Yang, Z., and Zhang, X.: Influence of atmospheric conditions on the role of  
596 trifluoroacetic acid in atmospheric sulfuric acid-dimethylamine nucleation, *Atmos. Chem. Phys.*, 21,  
597 6221-6230, 2021.

598 Long, B., Chang, C.-R., Long, Z.-W., Wang, Y.-B., Tan, X.-F., and Zhang, W.-J.: Nitric acid catalyzed  
599 hydrolysis of  $\text{SO}_3$  in the formation of sulfuric acid: a theoretical study, *Chem. Phys. Lett.*, 581, 26-29,  
600 2013

601 Long, B., Wang, Y., Xia, Y., He, X., Bao, J. L., and Truhlar, D. G.: Atmospheric Kinetics: Bimolecular  
602 Reactions of Carbonyl Oxide by a Triple-Level Strategy, *J. Am. Chem. Soc.*, 143, 8402-8413, 2021.

603 Long, B., Xia, Y., Zhang, Y.-Q., and Truhlar, D. G.: Kinetics of sulfur trioxide reaction with water vapor  
604 to form atmospheric sulfuric acid, *J. Am. Chem. Soc.*, 145, 19866-19876, 2023.

605 Lovejoy, E. R. and Hanson, D. R.: Kinetics and products of the reaction  $\text{SO}_3 + \text{NH}_3 + \text{N}_2$ , *J. Phys. Chem.*,  
606 100, 4459-4465, 1996.

607 Ma, X., Zhao, X., Huang, Z., Wang, J., Lv, G., Xu, F., Zhang, Q., and Wang, W.: Determination of  
608 reactions between Criegee intermediates and methanesulfonic acid at the gas-liquid interface, *Sci. Total  
609 Environ.*, 707, 135804, 2020.

610 Mai, T. V. T., Duong, M. V., Nguyen, H. T., and Huynh, L. K.: Ab initio kinetics of the  $\text{HOSO}_2 + {}^3\text{O}_2 \rightarrow$   
611  $\text{SO}_3 + \text{HO}_2$  reaction, *Phys. Chem. Chem. Phys.*, 20, 6677-6687, 2018.

612 Manonmani, G., Sandhiya, L., and Senthilkumar, K. J. I. J. O. Q. C.: Hydrolysis of  $\text{HNSO}_2$ : A potential  
613 route for atmospheric production of  $\text{H}_2\text{SO}_4$  and  $\text{NH}_3$ , *Int. J. Quantum Chem.*, 120, e26182, 2020.

614 Mansour, K., Decesari, S., Bellacicco, M., Marullo, S., Santoleri, R., Bonasoni, P., Facchini, M. C.,

615 Ovadnevaite, J., Ceburnis, D., and O'Dowd, C.: Particulate methanesulfonic acid over the central  
616 Mediterranean Sea: source region identification and relationship with phytoplankton activity, *Atmos.*  
617 *Res.*, 237, 104837, 2020.

618 McGrath, M.J., Olenius, T., Ortega, I.K., Loukonen, V., Paasonen, P., Kurtén, T., Kulmala, M.,  
619 Vehkamäki, H., Atmospheric cluster dynamics code: a flexible method for solution of the birth-death  
620 equations. *Atmos. Chem. Phys.* 12, 2345-2355, 2012.

621 Meana-Pañeda, R., Zheng, J., Bao, J. L., Zhang, S., Lynch, B. J., Corchado, J. C., Chuang, Y.-Y., Fast, P.  
622 L., Hu, W.-P., and Liu, Y.-P.: Polyrate 2023: A computer program for the calculation of chemical reaction  
623 rates for polyatomics. New version announcement, *Comput Phys Commun*, 294, 108933, 2024.

624 Neese, F.: The ORCA program system, *WIREs Comput. Mol. Sci.*, 2, 73-78, 2012.

625 Parandaman, A., Perez, J. E., and Sinha, A.: Atmospheric decomposition of trifluoromethanol catalyzed  
626 by formic acid, *J. Phys. Chem. A*, 122, 9553-9562, 2018.

627 Pszona, M., Haupa, K., Bil, A., Mierzwicki, K., Szewczuk, Z., and Mielke, Z.: Clustering of sulfamic  
628 acid: ESI MS and theoretical study, *J. Mass Spectrom.*, 50, 127-135, 2015.

629 Rennebaum, T., van Gerven, D., Sebastian, S. S., and Wickleder, M. S.: Hydrazine sulfonic acid,  $\text{NH}_3\text{NH}$   
630  $(\text{SO}_3)$ , the bigger sibling of sulfamic acid, *CHEM-EUR J*, 30, e202302526, 2024.

631 Saltzman, E., Savoie, D., Prospero, J., and Zika, R.: Methanesulfonic acid and non-sea-salt sulfate in  
632 Pacific air: Regional and seasonal variations, *J. Atmos. Chem.*, 4, 227-240, 1986.

633 Sarkar, S., Mallick, S., Kumar, P., and Bandyopadhyay, B.: Isomerization of methoxy radical in the  
634 troposphere: Competition between acidic, neutral and basic catalysts, *Phys. Chem. Chem. Phys.*, 19,  
635 27848-27858, 2017.

636 Shang, D., Tang, L., Fang, X., Wang, L., Yang, S., Wu, Z., Chen, S., Li, X., Zeng, L., Guo, S., and Hu,  
637 M.: Variations in source contributions of particle number concentration under long-term emission control  
638 in winter of urban Beijing, *Environ. Pollut.*, 304, 119072, 2022.

639 Shen, J., Elm, J., Xie, H.-B., Chen, J., Niu, J., and Vehkamaki, H.: Structural effects of amines in  
640 enhancing methanesulfonic acid-driven new particle formation, *Environ. Sci. Technol.*, 54, 13498-13508,  
641 2020.

642 Shen, J., Xie, H.-B., Elm, J., Ma, F., Chen, J., and Vehkamaki, H.: Methanesulfonic acid-driven new  
643 particle formation enhanced by monoethanolamine: A computational study, *Environ. Sci. Technol.*, 53,  
644 14387-14397, 2019.

645 Chen, H.; Varner, M. E.; Gerber, R. B.; Finlayson-Pitts, B. J.: Reactions of methanesulfonic acid with  
646 amines and ammonia as a source of new particles in air, *J. Phys. Chem. B*, 120, 1526-1536, 2016.

647 Shi, Z., Ford, J., and Castleman Jr, A.: Cluster reactions of sulfur trioxide and ammonia, *Chemical*  
648 *physics letters*, 220, 274-280, 1994.

649 Tang, Y. S., Flechard, C. R., Dämmgen, U., Vidic, S., Djuricic, V., Mitosinkova, M., Uggerud, H. T., Sanz,  
650 M. J., Simmons, I., and Dragosits, U.: Pan-European rural monitoring network shows dominance of  $\text{NH}_3$   
651 gas and  $\text{NH}_4\text{NO}_3$  aerosol in inorganic atmospheric pollution load, *Atmos. Chem. Phys.*, 21, 875-914,  
652 2021.

653 Tsona Tchinda, N., Du, L., Liu, L., and Zhang, X.: Pyruvic acid, an efficient catalyst in  $\text{SO}_3$  hydrolysis  
654 and effective clustering agent in sulfuric-acid-based new particle formation, *Atmos. Chem. Phys.*, 22,  
655 1951-1963, 2022.

656 Van Stempvoort, D., Spoelstra, J., Brown, S., Robertson, W., Post, R., and Smyth, S.: Sulfamate in  
657 environmental waters, *Sci. Total Environ.*, 695, 133734, 2019.

658 VandeVondele, J. and Hutter, J.: Gaussian basis sets for accurate calculations on molecular systems in

659 gas and condensed phases, *J. Chem. Phys.*, 127, 114105, 2007.

660 VandeVondele, J., Krack, M., Mohamed, F., Parrinello, M., Chassaing, T., and Hutter, J.: Quickstep: Fast  
661 and accurate density functional calculations using a mixed Gaussian and plane waves approach, *Comput.*  
662 *Phys. Commun.*, 167, 103-128, 2005.

663 Wang, R., Cheng, Y., Chen, S., Li, R., Hu, Y., Guo, X., Zhang, T., Song, F., and Li, H.: Reaction of SO<sub>3</sub>  
664 with H<sub>2</sub>SO<sub>4</sub> and its implications for aerosol particle formation in the gas phase and at the air-water  
665 interface, *Atmos. Chem. Phys.*, 24, 4029-4046, 2024.

666 Wang, S., Nan, J., Shi, C., Fu, Q., Gao, S., Wang, D., Cui, H., Saiz-Lopez, A., and Zhou, B.: Atmospheric  
667 ammonia and its impacts on regional air quality over the megacity of Shanghai, China, *Sci. Rep.*, 5, 15842,  
668 2015.

669 Warner, J. X., Wei, Z., Strow, L. L., Dickerson, R. R., Nowak, J. B., and Physics: The global tropospheric  
670 ammonia distribution as seen in the 13-year AIRS measurement record, *Atmos. Chem. Phys.*, 16, 5467-  
671 5479, 2016.

672 Xue, J., Shao, X., Li, J., Li, J., Trabelsi, T., Francisco, J. S., and Zeng, X.: Observation of the Water-  
673 HNO<sub>2</sub> complex, *J. Am. Chem. Soc.*, 146, 5455-5460, 2024.

674 Yu, X., Shen, L., Hou, X., Yuan, L., Pan, Y., An, J., and Yan, S.: High-resolution anthropogenic ammonia  
675 emission inventory for the Yangtze River Delta, China, *CHEMOSPHERE*, 251, 126342, 2020.

676 Zhang, J. and Dolg, M.: AB Cluster: the artificial bee colony algorithm for cluster global optimization,  
677 *Phys. Chem. Chem. Phys.*, 17, 24173-24181, 2015.

678 Zhang, R., Khalizov, A., Wang, L., Hu, M., and Xu, W.: Nucleation and growth of nanoparticles in the  
679 atmosphere, *Chem. Rev.*, 112, 1957-2011, 2012.

680 Zhang, R., Shen, J., Xie, H. B., Chen, J., and Elm, J.: The role of organic acids in new particle formation  
681 from methanesulfonic acid and methylamine, *Atmos. Chem. Phys.*, 22, 2639-2650, 2022.

682 Zhang, T., Wen, M., Cao, X., Zhang, Y., Zeng, Z., Guo, X., Zhao, C., Lily, M., and Wang, R.: The  
683 hydrolysis of NO<sub>2</sub> dimer in small clusters of sulfuric acid: A potential source of nitrous acid in  
684 troposphere, *Atmos. Environ.*, 243, 117876, 2020.

685 Zhang, T., Wen, M., Ding, C., Zhang, Y., Ma, X., Wang, Z., Lily, M., Liu, J., and Wang, R.: Multiple  
686 evaluations of atmospheric behavior between Criegee intermediates and HCHO: Gas-phase and gas-  
687 liquid interface reaction, *J. Environ. Sci.*, 127, 308-319, 2023.

688 Zhang, T., Wen, M., Zhang, Y., Lan, X., Long, B., Wang, R., Yu, X., Zhao, C., and Wang, W.: Atmospheric  
689 chemistry of the self-reaction of HO<sub>2</sub> radicals: stepwise mechanism versus one-step process in the  
690 presence of (H<sub>2</sub>O)<sub>n</sub> (n = 1-3) clusters, *Phys. Chem. Chem. Phys.*, 21, 24042-24053, 2019.

691 Zhang, T., Zhang, Y., Tian, S., Zhou, M., Liu, D., Lin, L., Zhang, Q., Wang, R., and Muthiah, B.: Possible  
692 atmospheric source of NH<sub>2</sub>SO<sub>3</sub>H: the hydrolysis of HNO<sub>2</sub> in the presence of neutral, basic, and acidic  
693 catalysts, *Phys. Chem. Chem. Phys.*, 24, 4966-4977, 2022.

694 Zhang, X., Lian, Y., Tan, S., Yin, S., and Physics: Organ sulfate produced from consumption of SO<sub>3</sub>  
695 speeds up sulfuric acid-dimethylamine atmospheric nucleation, *Atmos. Chem. Phys.*, 24, 3593-3612,  
696 2024.

697 Zhang, Y., Wang, Z., Wang, H., Cheng, Y., Zhang, T., Ou, T., and Wang, R.: Atmospheric chemistry of  
698 NH<sub>2</sub>SO<sub>3</sub>H in polluted areas: an unexpected isomerization of NH<sub>2</sub>SO<sub>3</sub>H in acid-polluted regions, *J. Phys.*  
699 *Chem. A*, 127, 8935-8942, 2023.

700 Zhao, X., Shi, X., Ma, X., Zuo, C., Wang, H., Xu, F., Sun, Y., and Zhang, Q.: 2-Methyltetrol sulfate ester-  
701 initiated nucleation mechanism enhanced by common nucleation precursors: A theory study, *Sci. Total*  
702 *Environ.*, 723, 137987, 2020.

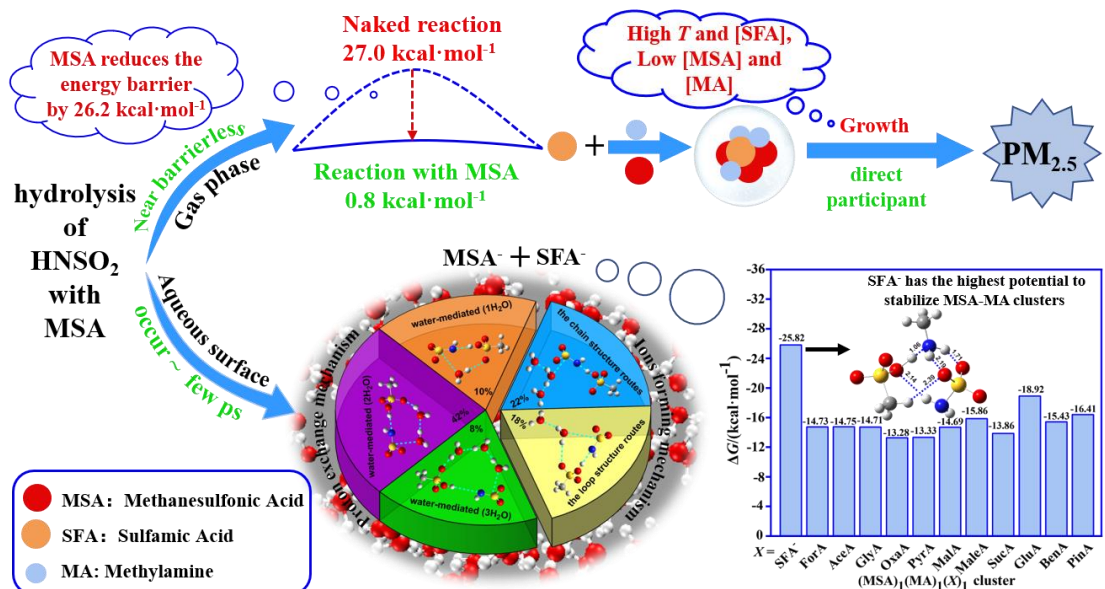
703 Zhao, Y. and Truhlar, D. G.: The M06 suite of density functionals for main group thermochemistry,  
704 thermochemical kinetics, noncovalent interactions, excited states, and transition elements: two new  
705 functionals and systematic testing of four M06-class functionals and 12 other functionals, *Theor. Chem.  
706 Acc.*, 120, 215-241, 2008.

707 Zhong, J., Kumar, M., Francisco, J. S., and Zeng, X. C.: Insight into chemistry on cloud/aerosol water  
708 surfaces, *Acc. Chem. Res.*, 51, 1229-1237, 2018.

709 Zhong, J., Kumar, M., Zhu, C. Q., Francisco, J. S., and Zeng, X. C.: Frontispiece: surprising stability of  
710 larger criegee intermediates on aqueous interfaces, *ANGEW CHEM INT EDIT*, 56, 7740-7744, 2017.

711 Zhong, J., Li, H., Kumar, M., Liu, J., Liu, L., Zhang, X., Zeng, X. C., and Francisco, J. S.: Mechanistic  
712 insight into the reaction of organic acids with  $\text{SO}_3$  at the air-water interface, *ANGEW CHEM INT EDIT.*,  
713 131, 8351-8355, 2019.

714 Zhu, C., Kumar, M., Zhong, J., Li, L., Francisco, J. S., and Zeng, X. C.: New mechanistic pathways for  
715 Criegee-water chemistry at the air/water interface, *J. Am. Chem. Soc.*, 138, 11164-11169, 2016.



## Graphical abstract

## Figure Captions

**Fig. 1** The potential energy profile ( $\Delta G$ ) for the hydrolysis reaction of  $\text{HNSO}_2$  with MSA at the CCSD(T)-F12/cc-pVDZ-F12//M06-2X/6-311++G(2df,2pd) level of theory

**Fig. 2** BOMD simulation trajectories and snapshots of  $\text{NH}_2\text{SO}_3^-$  and  $\text{H}_3\text{O}^+$  ions forming mechanism (chain structure (a) and loop-structure (b)) in the  $\text{HNO}_2$  hydrolysis with MSA at the air-water interface

**Fig. 3** BOMD simulation trajectories and snapshots of proton exchange mechanism in MSA-mediated hydration  $\text{HNSO}_2$  with one (a) and two (b) water molecules at the air-water interface

**Fig. 4** Percentages of different mechanisms for the  $\text{HNO}_2$  hydrolysis with MSA at the air-water interface observed in BOMD simulations

**Fig. 5** ESP-mapped molecular vdW surface of MA, SFA and MSA molecules at M06-2X/6-311++G(2df,2pd) level of theory. Surface local minima and maxima of ESP of the different functional groups in MA, SFA and MSA molecules are represented as blue and yellow spheres, respectively. The values of maximum and minimum are shown in kcal mol<sup>-1</sup> in the parentheses. The green, red and blue arrows refer to the tendencies to form hydrogen bonds and proton transfer events, respectively. (green = carbon, red = oxygen, blue = nitrogen, yellow = sulfur and white = hydrogen.)

**Fig. 6** The  $J$  ( $\text{cm}^{-3} \text{s}^{-1}$ ) (a) and  $R$  (b) versus [SFA] with  $[\text{MSA}] = 10^6 \text{ molecules cm}^{-3}$ ,  $[\text{MA}] = 2.5 \times 10^8 \text{ molecules cm}^{-3}$  and four different temperatures (green line: 298.15 K, blue line: 278.15 K, red line: 258.15 K, black line: 238.15 K).

**Fig. 7** The  $J$  ( $\text{cm}^{-3} \text{s}^{-1}$ ) (a) and  $R$  (b) as a function of [MSA] with [SFA] =  $10^8$  molecules  $\text{cm}^{-3}$  and three different [MA] (black line:  $[\text{MA}] = 2.5 \times 10^7$  molecules  $\text{cm}^{-3}$ , red line:  $[\text{MA}] = 2.5 \times 10^8$  molecules  $\text{cm}^{-3}$ , blue line:  $[\text{MA}] = 2.5 \times 10^9$  molecules  $\text{cm}^{-3}$ ) at 278.15 K.

**Fig. 8** Main cluster formation mechanism of MSA-MA-SFA-based system at 278.15 K,  $[MSA] = 10^7$  molecules $\cdot$ cm $^{-3}$ ,  $[MA] = 2.5 \times 10^8$  molecules $\cdot$ cm $^{-3}$ , and  $[SFA] = 10^6$  molecules $\cdot$ cm $^{-3}$ . (a) The black arrows indicate the pure MSA-MA-based growth pathways. Blue arrows represent the pathways containing SFA. The influence of (b) temperature, (c) [SFA] and [MSA] on the relative contribution of the pure MSA-MA-based clustering pathway and the SFA participation pathway to the system flux is analyzed. Others in (b), and (c) indicate that the pathway contribution of the cluster growing out of the studied system is less than 5%

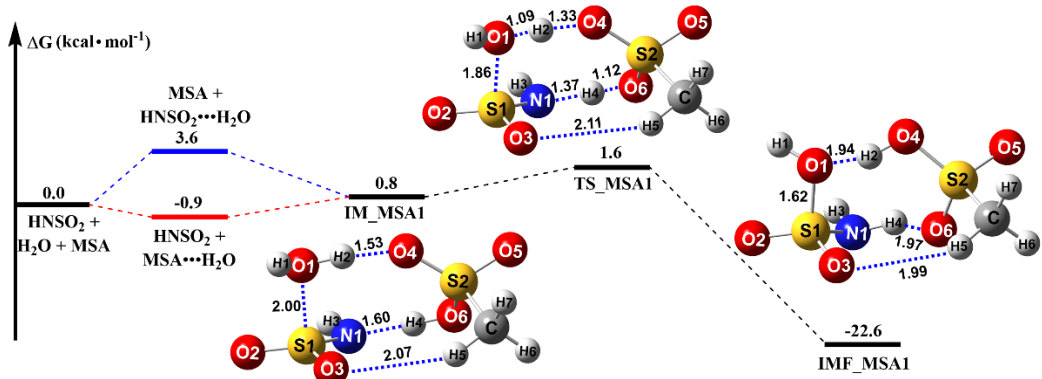
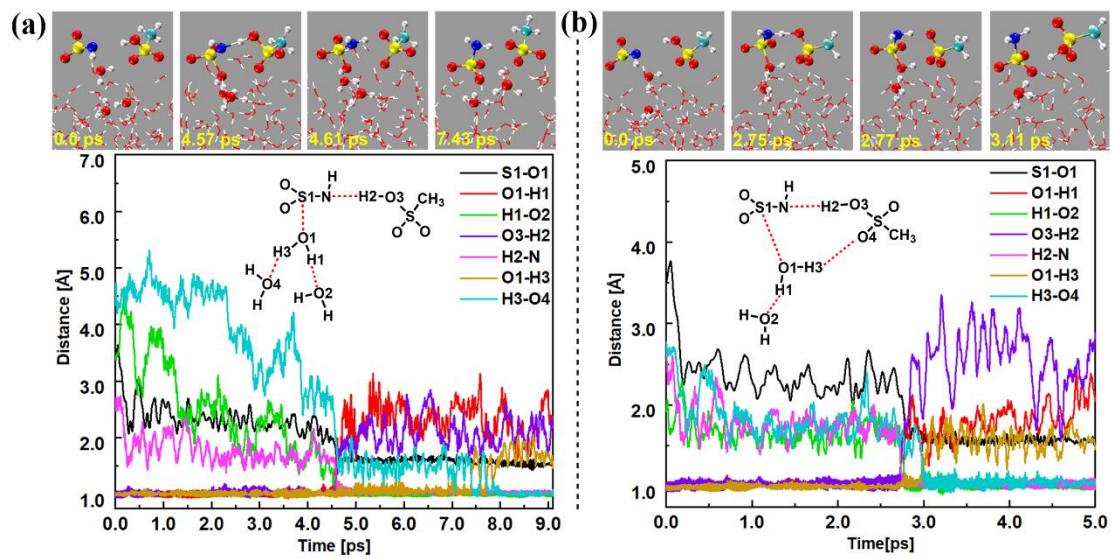


Fig. 1

761

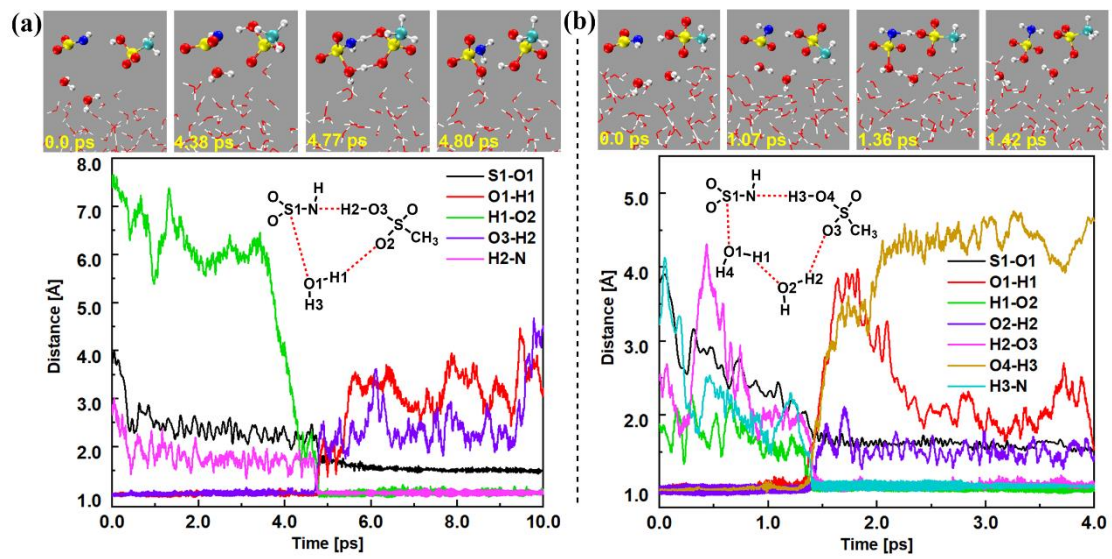
762



763

764

Fig. 2



765

766

767

Fig. 3

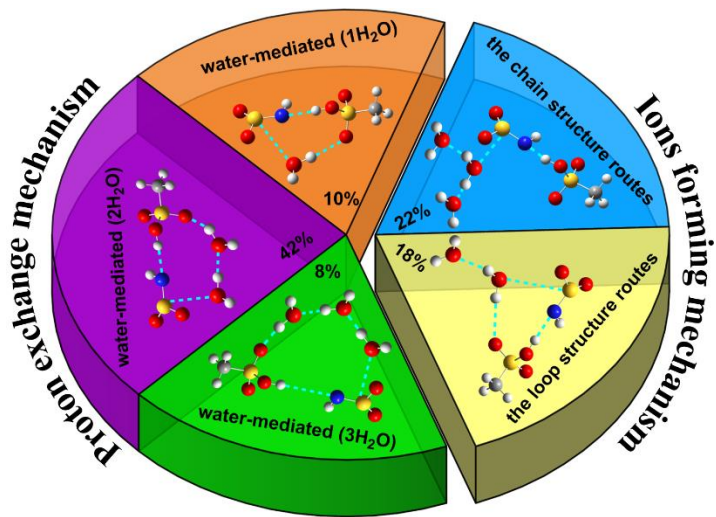
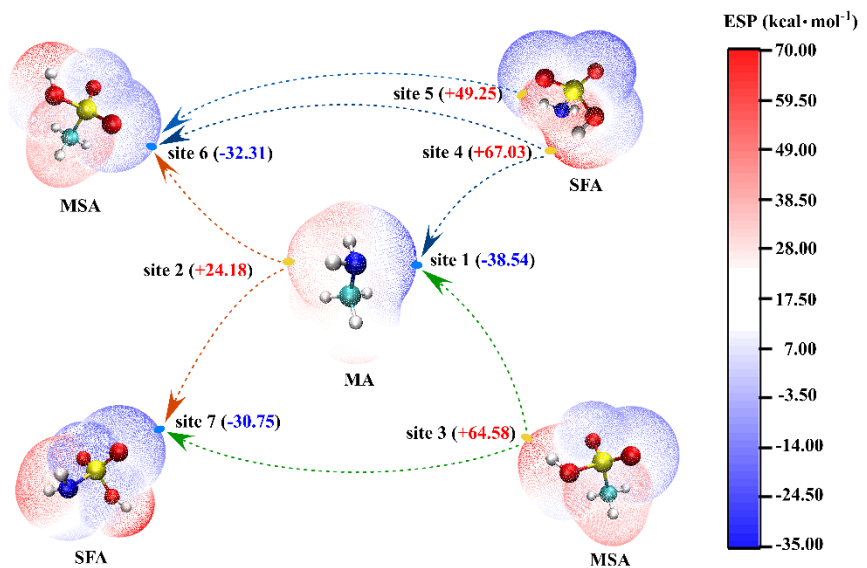


Fig. 4

768

769



770

771

Fig. 5

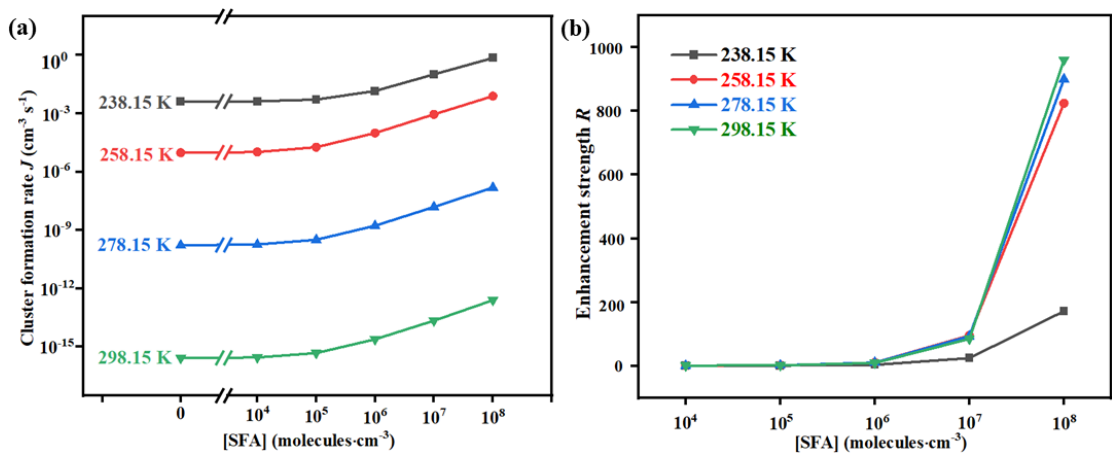


Fig. 6

772

773

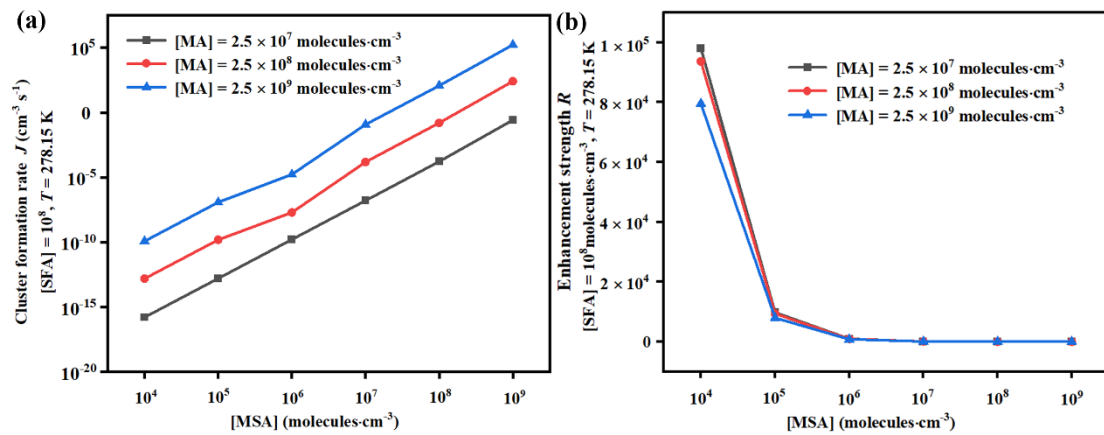


Fig. 7

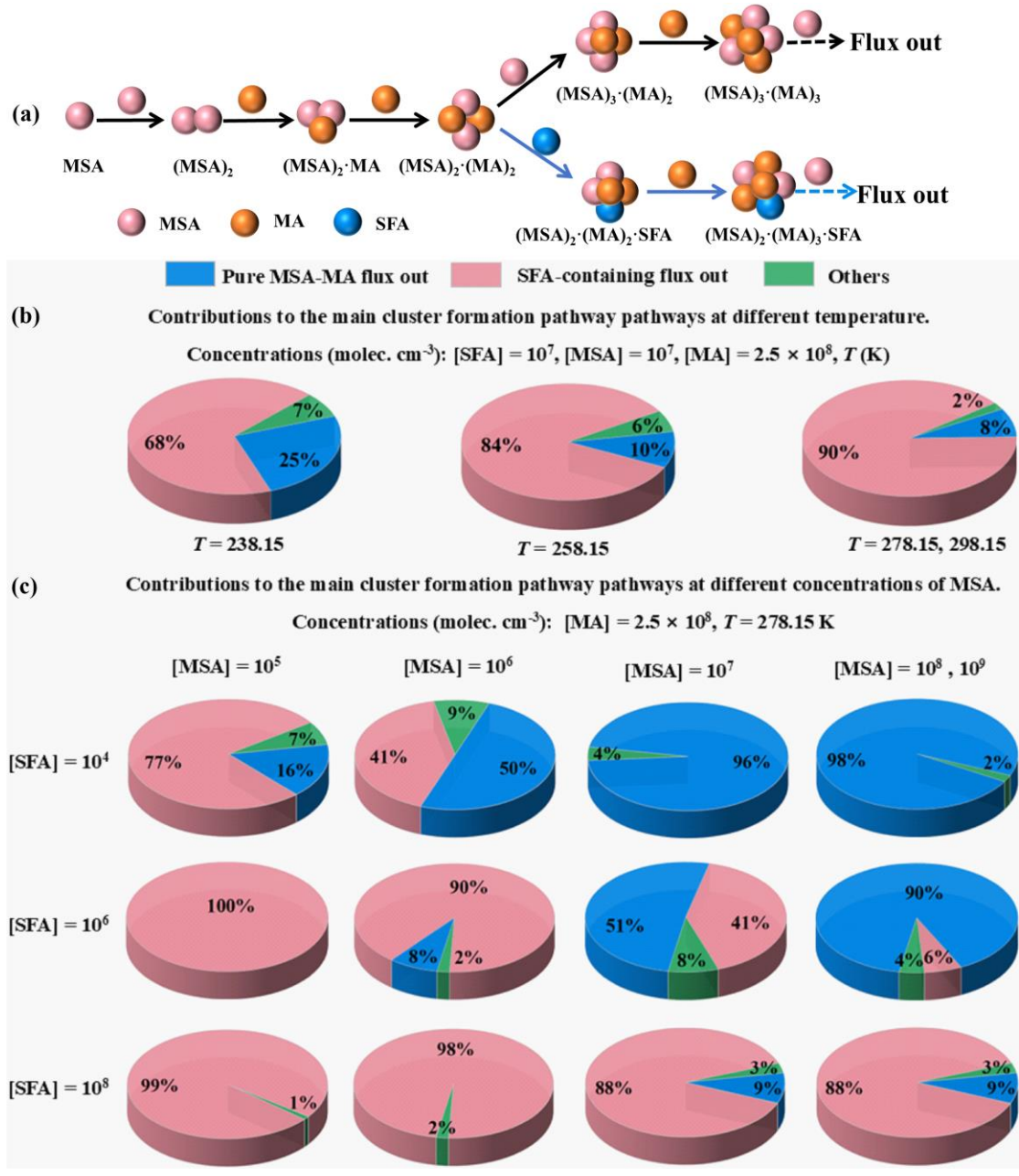


Fig. 8

**Table 1** Rate coefficients ( $k$ ,  $\text{cm}^3 \cdot \text{molecule}^{-1} \cdot \text{s}^{-1}$ ) and effective rate constants ( $k'$ ,  $\text{cm}^3 \cdot \text{molecule}^{-1} \cdot \text{s}^{-1}$ ) for the hydrolysis of  $\text{HNSO}_2$  with  $\text{H}_2\text{O}$  and MSA calculated by master equation within the temperature range of 213–320 K and altitude range of 0–15 km

Altitude	0 km				5 km				10 km				15 km			
T/K	280	290	298	300	310	320	329	330	340	350	360	370	380	390	399	408
$k_{\text{WM}}$	$7.64 \times 10^{-13}$	$6.45 \times 10^{-13}$	$5.63 \times 10^{-13}$	$5.44 \times 10^{-13}$	$4.59 \times 10^{-13}$	$3.88 \times 10^{-13}$	$3.09 \times 10^{-13}$	$2.32 \times 10^{-13}$	$1.69 \times 10^{-13}$	$1.09 \times 10^{-12}$	$7.72 \times 10^{-12}$	$5.50 \times 10^{-12}$	$3.50 \times 10^{-11}$	$2.22 \times 10^{-11}$	$1.50 \times 10^{-11}$	$2.12 \cdot 10^{-11}$
	$3.08 \times 10^{-11}$	$2.96 \times 10^{-11}$	$2.85 \times 10^{-11}$	$2.82 \times 10^{-11}$	$2.67 \times 10^{-11}$	$2.52 \times 10^{-11}$	$2.36 \times 10^{-11}$	$2.12 \times 10^{-11}$	$1.86 \times 10^{-11}$	$1.56 \times 10^{-11}$	$1.26 \times 10^{-11}$	$9.68 \times 10^{-11}$	$6.51 \times 10^{-11}$	$4.39 \times 10^{-11}$	$2.99 \times 10^{-11}$	$2.22 \times 10^{-11}$
$k_{\text{MSA}}$	$5.99 \times 10^{-18}$	$7.96 \times 10^{-18}$	$9.64 \times 10^{-18}$	$1.03 \times 10^{-17}$	$1.29 \times 10^{-17}$	$1.29 \times 10^{-17}$	$1.29 \times 10^{-17}$	$1.29 \times 10^{-17}$	$1.29 \times 10^{-17}$	$1.29 \times 10^{-17}$	$1.29 \times 10^{-17}$	$1.29 \times 10^{-17}$	$1.29 \times 10^{-17}$	$1.29 \times 10^{-17}$	$1.29 \times 10^{-17}$	$1.29 \times 10^{-17}$
	$1.19 \times 10^{-17}$	$1.58 \times 10^{-17}$	$1.99 \times 10^{-17}$	$2.07 \times 10^{-17}$	$2.60 \times 10^{-17}$	$3.12 \times 10^{-17}$	$3.64 \times 10^{-17}$	$4.16 \times 10^{-17}$	$4.68 \times 10^{-17}$	$5.21 \times 10^{-17}$	$5.73 \times 10^{-17}$	$6.24 \times 10^{-17}$	$6.75 \times 10^{-17}$	$7.26 \times 10^{-17}$	$7.79 \times 10^{-17}$	$8.31 \times 10^{-17}$
$k'$	$2.38 \times 10^{-17}$	$2.98 \times 10^{-17}$	$3.11 \times 10^{-17}$	$3.11 \times 10^{-17}$	$3.90 \times 10^{-17}$	$4.68 \times 10^{-17}$	$5.46 \times 10^{-17}$	$6.24 \times 10^{-17}$	$6.24 \times 10^{-17}$	$6.24 \times 10^{-17}$	$6.24 \times 10^{-17}$	$6.24 \times 10^{-17}$	$6.24 \times 10^{-17}$	$6.24 \times 10^{-17}$	$6.24 \times 10^{-17}$	$6.24 \times 10^{-17}$
	$3.17 \times 10^{-17}$	$3.97 \times 10^{-17}$	$4.14 \times 10^{-17}$	$4.14 \times 10^{-17}$	$5.21 \times 10^{-17}$	$6.24 \times 10^{-17}$	$7.26 \times 10^{-17}$	$8.31 \times 10^{-17}$	$8.31 \times 10^{-17}$	$8.31 \times 10^{-17}$	$8.31 \times 10^{-17}$	$8.31 \times 10^{-17}$	$8.31 \times 10^{-17}$	$8.31 \times 10^{-17}$	$8.31 \times 10^{-17}$	$8.31 \times 10^{-17}$
$k_{\text{RH}}$	$2.39 \times 10^{-17}$	$3.17 \times 10^{-17}$	$3.97 \times 10^{-17}$	$4.14 \times 10^{-17}$	$5.21 \times 10^{-17}$	$6.24 \times 10^{-17}$	$7.26 \times 10^{-17}$	$8.31 \times 10^{-17}$	$8.31 \times 10^{-17}$	$8.31 \times 10^{-17}$	$8.31 \times 10^{-17}$	$8.31 \times 10^{-17}$	$8.31 \times 10^{-17}$	$8.31 \times 10^{-17}$	$8.31 \times 10^{-17}$	$8.31 \times 10^{-17}$
	$2.97 \times 10^{-17}$	$3.96 \times 10^{-17}$	$4.97 \times 10^{-17}$	$5.18 \times 10^{-17}$	$6.50 \times 10^{-17}$	$7.79 \times 10^{-17}$	$9.08 \times 10^{-17}$	$10.37 \times 10^{-17}$								
$k'_{\text{MSA}}$	$4.81 \times 10^{-19}$	$2.50 \times 10^{-19}$	$1.57 \times 10^{-19}$	$1.40 \times 10^{-19}$	$7.90 \times 10^{-20}$	$4.60 \times 10^{-20}$	$1.96 \times 10^{-20}$	$2.37 \times 10^{-19}$	$1.30 \times 10^{-18}$							
	$1.62 \times 10^{-4}$	$6.42 \times 10^{-5}$	$3.16 \times 10^{-5}$	$2.69 \times 10^{-5}$	$1.22 \times 10^{-5}$	$5.90 \times 10^{-5}$	$3.01 \times 10^{-5}$	$1.38 \times 10^{-5}$	$1.38 \times 10^{-5}$	$1.38 \times 10^{-5}$	$1.38 \times 10^{-5}$	$1.38 \times 10^{-5}$	$1.38 \times 10^{-5}$	$1.38 \times 10^{-5}$	$1.38 \times 10^{-5}$	$1.38 \times 10^{-5}$
$k'_{\text{MSA}}/k_{\text{WM}}$		$k'_{\text{MSA}}$ and $k_{\text{MSA}}$ are respectively the rate constant for the hydrolysis of $\text{HNSO}_2$ with $\text{H}_2\text{O}$ and MSA; $k'_{\text{WM}}$ and $k_{\text{WM}}$ are respectively the effective rate constant for the hydrolysis of $\text{HNSO}_2$ with $\text{H}_2\text{O}$ and MSA.														

779 **Table 2.** Gibbs free energy ( $\Delta G$ ) for the formation of  $\text{SFA}^{-}\cdots\text{MSA}$ ,  $\text{SFA}^{-}\cdots\text{NA}$ ,  $\text{SFA}^{-}\cdots\text{OA}$ ,  
 780  $\text{H}_3\text{O}^{+}\cdots\text{MA}$ ,  $\text{MSA}^{-}\cdots\text{MSA}$ ,  $\text{MSA}^{-}\cdots\text{OA}$ , and  $\text{MSA}^{-}\cdots\text{NA}$ ,  $\text{MSA}^{-}\cdots\text{MA}$ ,  $(\text{MSA})_1\cdot(\text{MA})_1\cdot(X)_1$  at 298  
 781 K

	$\text{SFA}^{-}\cdots\text{MSA}$	$\text{SFA}^{-}\cdots\text{HNO}_3$	$\text{SFA}^{-}\cdots\text{OA}$	$\text{MSA}^{-}\cdots\text{MSA}$	$\text{MSA}^{-}\cdots\text{NA}$
$\Delta G$	-23.8	-21.5	-25.2	-23.9	-22.6
	$\text{MSA}^{-}\cdots\text{OA}$	$\text{MSA}^{-}\cdots\text{H}_3\text{O}^{+}$	$\text{MSA}^{-}\cdots\text{H}_3\text{O}^{+}$	$\text{MSA}^{-}\cdots\text{MA}$	
$\Delta G$	-25.8	-35.8	-57.9	-7.0 (-7.2) <sup>b</sup>	
	$\text{HCOOH}$ $\cdots\text{MSA}\cdots\text{MA}$	$\text{CH}_3\text{COOH}$ $\cdots\text{MSA}\cdots\text{MA}$	$\text{CHOCOOH}$ $\cdots\text{MSA}\cdots\text{MA}$	$\text{OA}$ $\cdots\text{MSA}\cdots\text{MA}$	
$\Delta G$	-14.7 (-15.8) <sup>a</sup>	-14.8 (-14.3) <sup>a</sup>	-14.7 (-15.6) <sup>a</sup>	-13.3 (-12.7) <sup>a</sup>	
	$\text{CH}_3\text{COCOOH}$ $\cdots\text{MSA}\cdots\text{MA}$	$\text{HOOCCH}_2\text{COOH}$ $\cdots\text{MSA}\cdots\text{MA}$	$\text{HOOC}(\text{CH})_2\text{COOH}$ $\cdots\text{MSA}\cdots\text{MA}$	$\text{HOOC}(\text{CH}_2)_2\text{COOH}$ $\cdots\text{MSA}\cdots\text{MA}$	
$\Delta G$	-13.3 (-13.0) <sup>a</sup>	-14.7 (-16.7) <sup>a</sup>	-15.9 (-15.3) <sup>a</sup>	-13.9 (-14.3) <sup>a</sup>	
	$\text{HOOC}(\text{CH}_2)_3\text{COOH}$ $\cdots\text{MSA}\cdots\text{MA}$	$\text{C}_6\text{H}_5(\text{COOH})$ $\cdots\text{MSA}\cdots\text{MA}$	$\text{C}_{10}\text{H}_{16}\text{O}_3$ $\cdots\text{MSA}\cdots\text{MA}$	$\text{SFA}^{-}$ $\cdots\text{MSA}\cdots\text{MA}$	
$\Delta G$	-18.9 (-17.9) <sup>a</sup>	-15.4 (-15.3) <sup>a</sup>	-16.4 (-15.3) <sup>a</sup>	-25.8	

782 <sup>a</sup> The value was taken from reference (Zhang, R., Shen, J., Xie, H. B., Chen, J., and Elm, J.: The role of organic acids  
 783 in new particle formation from methanesulfonic acid and methylamine, *Atmos. Chem. Phys.*, 22, 2639-2650,  
 784 10.5194/acp-22-2639-2022, 2022b.)

785 <sup>b</sup> The value was taken from reference (Zhong, J., Li, H., Kumar, M., Liu, J., Liu, L., Zhang, X., Zeng, X. C., and  
 786 Francisco, J. S.: Mechanistic Insight into the Reaction of Organic Acids with  $\text{SO}_3$  at the Air-Water Interface, *Angew. Chem. Int. Ed.*, 131, 8439-8443, 2019.)